REPORT DOCUMENTATION PAGE

AFRL-SR-BL-TR-01-

OO28

Public reporting burden for this collection of information is estimated to average 1 hour per response, including the time for reviewing data needed, and completing and reviewing this collection of information. Send comments regarding this burden estimate or any oth this burden to Department of Defense, Washington Headquarters Services, Directorate for Information Operations and Reports (070‹ 4302. Respondents should be aware that notwithstanding any other provision of law, no person shall be subject to any penalty for fai... ,g ... . currently valid OMB control number. **PLEASE DO NOT RETURN YOUR FORM TO THE ABOVE ADDRESS.**

1. REPORT DATE *(DD-MM-YYYY)* 09/26/2000	2. REPORT TYPE Final Report	3. DATES COVERED *(From - To)* 06/15/97-06/14/00

4. TITLE AND SUBTITLE "Polymer-based multi-mode coplanar asymmetrical unidirectional waveguide modulator for multi-wavelength"	5a. CONTRACT NUMBER F49620-97-1-0496
	5b. GRANT NUMBER
	5c. PROGRAM ELEMENT NUMBER

6. AUTHOR(S) Degui Sun, Xuejun Lu, John Martin Taboada, Michael Dubinovsky, Huajun Tang, Richard Lee, and Dr. Ray T. Chen	5d. PROJECT NUMBER
	5e. TASK NUMBER
	5f. WORK UNIT NUMBER

7. PERFORMING ORGANIZATION NAME(S) AND ADDRESS(ES) The University of Texas at Austin Microelectronics Research Center 10100 Burnet Rd., Bldg. 160 Austin, TX 78758	8. PERFORMING ORGANIZATION REPORT NUMBER For 26-0202-25

9. SPONSORING / MONITORING AGENCY NAME(S) AND ADDRESS(ES) AFOSR/NL Attn: Charles Y-C Lee 801 N. Randolph Street, Ste. 732 Arlington, VA 22203-1977	10. SPONSOR/MONITOR'S ACRONYM(S) ASOFR/NL
	11. SPONSOR/MONITOR'S REPORT NUMBER(S)

12. DISTRIBUTION / AVAILABILITY STATEMENT
Available for public release

13. SUPPLEMENTARY NOTES

14. ABSTRACT

A unidirectional electro-optic modulator based on polymeric highly multi-mode waveguides was constructed using the standard VLSI techniques. A high unidirectional coupling efficiency of 100% was achieved. A high modulation depth of 99% was also experimentally achieved at 633nm wavelength. The modulator was packaging enhanced by vertically configuring the guiding multi-mode waveguide and the dumping planar waveguide. The device packing density improved by a factor of two. Based on the same configuration, a packaging enhanced polarization-insensitive thermo-optic was also built. The switch operating at wavelengths of 632.8nm and 1.3μm has been demonstrated experimentally with extinction ratios of 21dB and 22dB, respectively. Such devices have an intrinsic wide optical bandwidth due to the large dynamic range of the phase-matching condition implied by the multi-mode waveguides.

These devices can be used in optoelectronic interconnects for data communications.

15. SUBJECT TERMS
Key words: multi-mode waveguide, electro-optic modulator, optoelectronic interconnects

16. SECURITY CLASSIFICATION OF:			17. LIMITATION OF ABSTRACT	18. NUMBER OF PAGES	19a. NAME OF RESPONSIBLE PERSON Ray T. Chen, Attn: Nancy Hard
a. REPORT U	b. ABSTRACT U	c. THIS PAGE U		51	19b. TELEPHONE NUMBER *(include area code)* 512/232-7543

Standard Form 298 (Rev. 8-98)
Prescribed by ANSI Std. Z39.18

DTIC QUALITY INSPECTED 3

COVER SHEET

"Polymer-based multi-mode coplanar asymmetrical unidirectional waveguide modulator for multi-wavelength"

Final Report

Contract No.: F49620-97-1-0496
Contract performance period: June 15, 1997 – June 14, 2000

Microelectronics Research Center
Department of Electrical and Computer Engineering
The University of Texas
Austin, Texas 78712-1084

Dr. Ray T. Chen
Principal Investigator
Phone: 512-471-7035
FAX: 512-471-8575
E-mail: raychen@uts.cc.utexas.edu

TABLE OF CONTENTS

LIST OF FIGURES

LIST OF TABLES

1. IDENTIFICATION AND SIGNIFICANCE OF THE INNOVATION

Employment of optoelectronic devices and components has become a necessity for many high-speed optical communication systems. Many existing and future devices and systems use such opto-electronic components as modulators, lasers, detectors, optical fibers and waveguides, to reach the upgraded performance that is not achievable using conventional microelectronic devices. One of the most successful examples is long-haul optical communications where tens of G-bit optical signals are transmitted using a single-mode fiber over thousands of miles. The success of optical fiber communications has triggered a plethora of basic research topics such as high speed laser diodes, detectors and passive and active materials for switching, modulating, transmitting and demodulating optical signals. Both analog and digital optical networks have been implemented to cover local area networks, cable TV networks, computer-to-computer networks and others. Laser diodes, electro-optic (EO) waveguide modulators, photo-detectors, optical fibers and waveguides have been investigated to cover single-mode systems [1]. Single-mode systems, such as long distance telecommunications [2] and high-speed computer-to-computer interconnections[3] are used mainly to provide the needed distance and bandwidth product. For many applications, however, the required distance and bandwidth are within the multi-mode optical interconnect systems [4]. When using an optical interconnect system with multi-mode fibers which have standard core sizes of 50 μm, 62.5 μm and higher, the optical system insertion loss is much lower than that of a single-mode interconnection system, due to the mode-match of discrete components [5,6]. Currently, all EO modulators such as Mach Zhender interferometers, directional couplers, digital optical switches, X-switches and Fabry Perot interferometers [5] are single-mode devices. There are several fundamental issues which need to be addressed to come up with a multi-mode EO modulator suitable for a multimode interconnect system. First, the working principles of existing EO modulators are intrinsically single-mode. An optimized interaction length can be provided only to a specific mode even though the waveguide under consideration is a multimode guide. Second, the conventional waveguide fabrication methods on $LiNbO_3$ and III-V semiconductor substrates are not feasible to fabricate a channel waveguide with a waveguide depth compatible with a multi-mode fiber. Finally, the working mechanism for multimode waveguide modulators aimed at multi-mode interconnect systems has not yet been found.

In this program, we build an electro-optic polymer-based coplanar asymmetrical unidirectional multimode waveguide modulator for a low-loss multimode optical interconnect system. Unlike the waveguide fabrication methods for inorganic crystal, the active polymer thin films can be spin-coated on any surface. By choosing appropriate solvents, an EO polymer film with a thickness compatible with a multimode fiber can be realized by a multiple-coating process. The device

external device with which it is to be interconnected, and Waveguide B is designed to be a lossy guide with enough modes to reduce the voltage needed to couple the optical guided wave from Waveguide A. The high loss of Waveguide B ensures the unidirectional coupling from A to B. The total number of modes in guide B is carefully designed to provide not only a low driving voltage but also a high extinction ratio, i.e., large modulation depth. To achieve
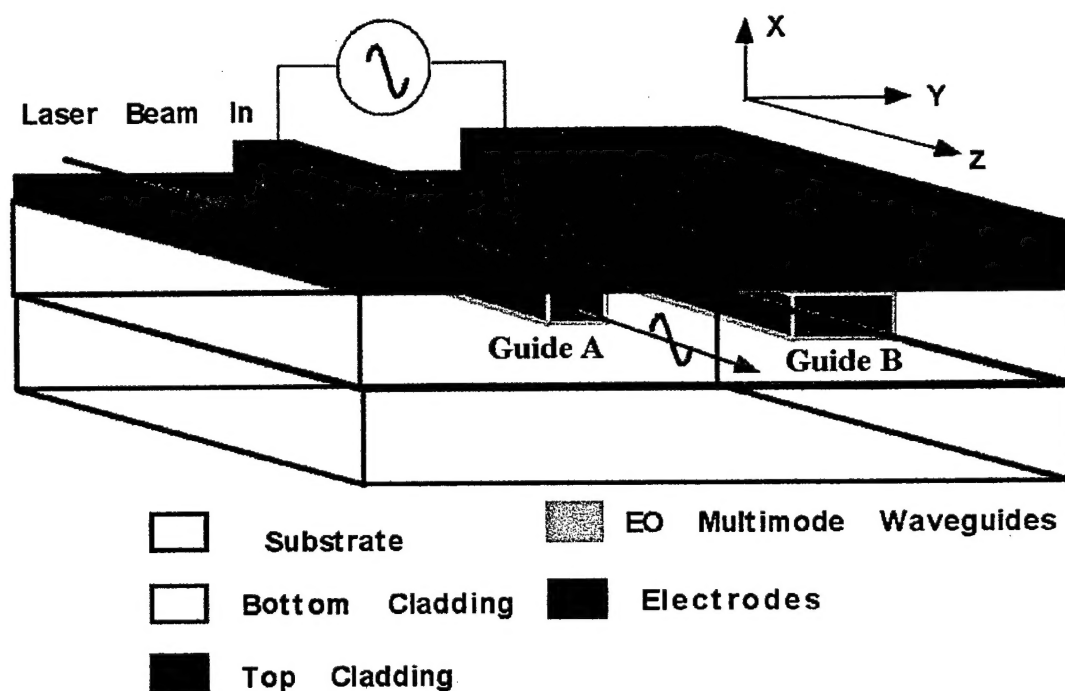
Figure 1.1   Electro-optic Polymer-based Coplanar Asymmetrical Unidirectional Multimode Waveguide Modulators

this goal, the size of the core regions for Guide A and Guide B and the index differences from the sounding areas are pivotal in optimizing the device. For each mode in Guide A, there is a corresponding mode or modes with the effective indices in Guide B so that an energy transfer occurs. Such an energy transfer can be either terminated or activated by perturbing the waveguide effective indices through applying an external electric field. Guide B is purposely fabricated to be highly lossy such that the optical energy coupled from Guide A to Guide B will be "dumped" through the loss mechanism, resulting in the unidirectional coupling.

This provides a low-loss coupling mechanism by matching the mode profile of photonic devices such as multimode fibers and photo-detectors while maintaining a very low switching voltage (<10 volts) for unidirectional coupling with a high extinction ratio (> 90%). The index of refraction of the EO

2

This provides a low-loss coupling mechanism by matching the mode profile of photonic devices such as multimode fibers and photo-detectors while maintaining a very low switching voltage (<10 volts) for unidirectional coupling with a high extinction ratio (> 90%). The index of refraction of the EO polymeric materials such as LD-3, Dispersive Red-19 and EO polyimide are close to that of glass fiber. As a result, a low loss coupling is expected for both lateral and transverse dimensions.

In summary, multimode EO/TO switches/modulators have the following advantages:

(1) Compatibility with data communication applications for short interconnection distance.

(2) Coupling light between multi-mode waveguides and multi- mode optical fibers is usually easy and efficient.

(3) Relatively easier fabrication conditions and packaging.

(4) Possible wide-band operation due to large dynamic range of the phase match conditions introduced by multi-mode waveguides.

1. OVERVIEW OF THE ACHIEVEMENTS

We have investigated the feasibility of polymeric modulators and switches based on multi-mode waveguide and enhanced the device packing density by building three different devices: (1) a co-planar polymeric EO modulator, (2) a polymeric thermo-optic switch with guiding waveguide and dumping planar waveguide vertically configured, (3) a channel array multi-mode electro-optical modulator with guiding channels and dumping layer vertically configured. The six major technical achievements are:

1. We have explored theoretically the device concept of EO modulator based on multi-mode waveguide. We have analyzed and calculated the unidirectional coupling mechanism, which is a key concept for building modulator and switches based on multi-mode waveguide.

2. We have investigated different NLO polymers that can be used in building thermo-optic and EO modulators. We have also developed a reliable contact poling method that can give sufficient EO coefficient for building EO devices.

3. We have developed a co-planar EO modulator based on the unidirectional coupling mechanism. This modulator is compatible with data communication. A high unidirectional coupling efficiency of ~100% and modulation depth of 90% have been achieved.

4. We have built a novel multi-mode waveguide thermo-optical switch based on the same unidirectional coupling mechanism. The thermo-optic switch has an intrinsic wide optical bandwidth due to the large dynamic range of the phase-matching condition implied by the multi-mode waveguides. The thermo-optic switch is also polarization insensitive due to the direction independence of thermal effect ($\partial n/\partial T$).

5. We have improved the design structure for dense switch/modulator configuration by vertically configuring the guiding channel and dumping channel. This design can improve the device packing density by a factor of two.

6. We have built a channel array multi-mode electro-optical modulator with guiding channels and dumping layer vertically configured. This modulator has a device packing density of 40 channels/cm, which matches the 250μm fiber array spacing.

3. DETAILED RESULTS

3.1 Design of Electro-optic Modulator Based on Multi-mode Waveguides

Unlike devices based on single mode waveguides, the design of an electro-optic modulator based on multi-mode waveguides must control phase matching conditions of different modes simultaneously. Because of the different effective indices, coupling lengths of different modes between guiding channel and dumpling channel are not the same. These differences will degrade the extinction ratio of a modulator/switch. In the worst case, the modulator/switch may not work at all. We employed a unidirectional coupling mechanism in the device design, which ensures the uniformity of the different modes' behaviors under the modulation voltage. The principle of the unidirectional coupling mechanism is shown in Fig. 3.1.1.

The idea is to make the dumping channel highly lossy. Light coupled from the guiding channel will be greatly dumped, thus minimizing the opposite coupling, i.e. coupling from dumpling channel to guiding channel. As a result, all different modes dumped after a certain distance when the phase match conditions are satisfied. The distance depends on the separation of two channels and their index difference. Thus the unidirectional coupling mechanism is achieved.
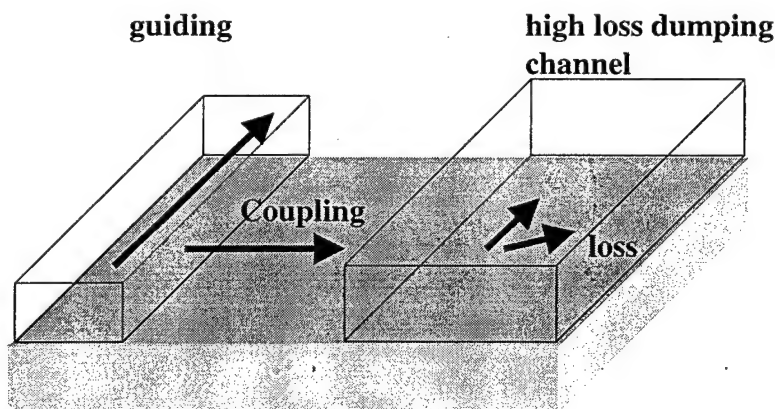
Fig. 3.1.1 Schematic view of unidirectional coupling mechanism

3.1.2 Theoretical Analysis of Electro-optic Modulator Based on Multi-mode Waveguides

In deriving the theoretical result, we have assumed that the incident laser beam either from an edge-emitting laser or from a vertical cavity surface emitting laser (VCSEL) is with a TEM_{00} Gaussian profile.

The schematic view of the device is shown in Fig. 3.1.2.
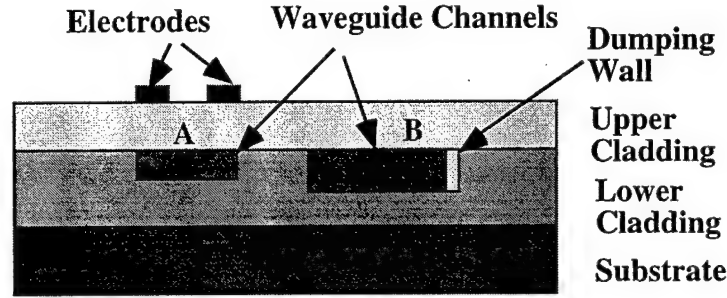
Fig. 3.1.2 Schematic view of the device

To achieve full understanding of the entire coupling process between Guide A and Guide B, we must calculate the coupling coefficient from the (j,m)th mode of Guide A to the (j',m')th mode of Guide B, , $k_{j'm',jm}$, or its inverse coefficient $k_{jm,\bar{j}m'}$.[7-15]. In accordance with the coupled-mode theory, these two coupling coefficients can be defined by

$$k_{j'm',jm} = \frac{\omega \Delta n^2}{4} \int_A E_{jm}^a(y) E_{j'm'}^b(y) dy \text{, and} \tag{1}$$

$$k_{jm,j'm'} = \frac{\omega \Delta n^2}{4} \int_B E_{jm}^a(y) E_{j'm'}^b(y) dy \tag{2}$$

In Eqns.(1) and (2), ω is the angular frequency, Δn if the effective index difference of the two modes under consideration, and $E_{jm}^a(y)$ and $E_{j'm'}^b(y)$ are the mode profiles of the (j,m)th and the (j',m')th modes associated with Guide A and Guide B, respectively. Combining the coupled-mode theories for symmetrical parallel waveguides and for asymmetrical parallel waveguides[12-14], the coupling efficiency from the (j,m)th mode of Guide A to the (j',m')th mode of Guide B can be expressed as:

$$\eta_{j'm',jm} = \frac{k_{j'm',jm}^2}{\psi_{jm,j'm'}^2} \sin^2(\psi_{jm,\bar{j}m'}L) \tag{3}$$

where L is the interaction length, and $\psi_{jm,j'm'}$ is defined by

$$\psi_{jm,j'm'} = (k_{jm,j'm'} \cdot k_{j'm',jm} + \Delta^2_{jm,j'm'})^{1/2}, \text{ and} \tag{4}$$

where $\Delta_{jm,j'm'} = k|N_{jm} - N_{j'm'}|/2$. Based on Eqns. (3) and (4), the sum of normalized coupling efficiency from one mode of Guide A to all the "phase-matched" modes in Guide B can be expressed as:

$$\eta_{jm} = \frac{\sum\limits_{j',m'}^{J',M'} P^R_{j'm'} \eta_{j'm',jm}}{\sum\limits_{j',m'}^{J',M'} P^R_{j'm'}} \tag{5}$$

where j' and m' represent the subscript of the mode $\Psi_{j'm'}$ where j' and m' are integers covering all modes to J' and M' within Guide B, and $P^R_{j'm'}$ is the normalized optical intensity and $\eta_{j'm',jm}$ is defined by Eqn.(3). Based on Eqn. (5), the sum of the normalized coupling efficiencies from all the guided modes in Guide A to all the modes in Guide B, i.e., total coupling efficiency, can be written as:

$$\eta_t = \frac{\sum\limits_{j,m}^{J,M} P^R_{jm} \eta_{jm}}{\sum\limits_{j,m}^{J,M} P^R_{jm}} \tag{6}$$

where j and m represent the subscript of the mode ψ_{jm} where j and m are integers covering all modes to J and M within Guide A. With Eqns. (3) through (5), taking the waveguide separation S as 5.0 μm together with other parameters, we obtain the sum of normalized coupling efficiencies as a function of the interaction length from one mode of Guide A to all the modes of Guide B. Since the incoming laser beam is a TEM_{00} Gaussian beam which is an even function, the coupling efficiencies are 0% for all ψ_{jm}s in Guide A with either j=1,3,5,⋯or m=1,3,5,⋯. To provide a unidirectional coupling, Guide B shown in Figure 2.2 has to be extremely lossy. Such a condition can be implemented by doping highly absorptive material at the wavelength of interest. For example, LDS 821, IR 144 and HITC[16] are all highly absorptive in the 850 nm (>40 dB/cm) that the most popular wavelength for vertical cavity surface emitting lasers (VCSELs) is located. The unidirectional coupling can be realized once a photon is coupled from Guide A to Guide B. Guide B traps the photons through the proposed loss mechanism.

7

3.1.3. Coupled Mode Equation for Unidirectional Coupling

Unidirectional coupling is required in order to achieve a higher modulation depth for the proposed multimode EO modulator. In this section, the coupled mode equation addressing the power transfer is presented for all coupling scenarios. Assuming A_{jm} and $B_{j'm'}$ are the complex amplitudes of the (j,m)th mode in Guide A and the (j',m')th mode in Guide B, respectively, and $\alpha_{j'm'}$ is the purposely imposed loss coefficient corresponding to the mode (j',m') in Guide B, a set of differential equations describing the special coupling process can be expressed as follows:

$$\frac{dA_{jm}}{dz} = i\beta_{jm}A_{jm} + k_{jm,j'm'}B_{j'm'}, \text{ and} \tag{7a}$$

$$\frac{dB_{j'm'}}{dz} = i\beta_{j'm'}B_{j'm'} + k_{j'm',jm}A_{jm} - \alpha_{j'm}B_{j'm'} \tag{7b}$$

In Eqns(7a) and (7b), z is the waveguide propagation direction and β_{jm} and $\beta_{j'm'}$ are the corresponding wave vectors in Guide A and Guide B, respectively. Solving these two differential equations, we have an expression of the coupling efficiency from the (j,m)th mode of Guide A to the (j',m')th mode of Guide B as defined by

$$\eta^{\alpha}_{j'm',jm} = \frac{k^2_{j'm',jm}}{\psi^2_{jm,j'm'}} e^{-\alpha_{j'm}L} \cdot \sin^2(\psi_{jm,j'm'}L) \tag{8}$$

where $\psi_{jm,j'm'}$ is defined in Eqn(4) and L is the waveguide interaction length. The dumping rate $D_{jm,j'm}$ corresponding to the (j'm')th mode in Guide B can be written as:

$$D_{jm,j'm'} = \frac{k^2_{j'm',jm}}{\psi^2_{jm,j'm'}}(1 - e^{-\alpha_{j'm}L}) \cdot \sin^2(\psi_{jm,j'm'}L)$$

$$= \frac{k^2_{j'm',jm}}{\psi^2_{jm,j'm'}} \tau_{j'm'} \cdot \sin^2(\psi_{jm,j'm'}L) \tag{9}$$

where

$$\tau_{j'm'} = 1 - e^{-\alpha_{j'm}L} \tag{10}$$

8

To implement the dumping effect, Guide B is made to be lossy by doping it through an absorptive material.

With Eq. (8), the formula of the dumping efficiency from the (j,m)th mode in Guide A to the (j',m')th mode in Guide B is derived as [17,18]:

$$\eta^d_{j'm',jm} = \sum_{n=0}^{N_L} \frac{k^2_{j'm',jm}}{\psi^2_{jm,j'm'}} \tau_{j'm'} \cdot \sin^2[\psi_{jm,j'm'}(n+1)\Delta L] \cdot [1 - \frac{k^2_{j'm',jm}}{\psi^2_{jm,j'm'}} \tau_{j'm'} \cdot \sin^2(\psi_{jm,j'm'} n\Delta L)]$$

(11)

where ΔL is a selected length within which the dumped energy can be treated as a constant, and N_L is defined by

$$N_L = int(\frac{L}{\Delta L})$$

(12)

In Eqn.(12) int(x) means to take an integral close to x.

In viewing Eqn.(5), the sum of the normalized dumping efficiency from one mode of Guide A to all the modes of Guide B can be defined by

$$\eta^d_{jm} = \frac{\sum\limits_{j',m'}^{J',M'} P^R_{j'm'} \eta^d_{j'm',jm}}{\sum\limits_{j',m'}^{J',M'} P^R_{j'm'}},$$

(13)

where $\eta^d_{j'm',jm}$ is the dumping efficiency from the (j,m)th mode of Guide A to the $(j'm')$th mode of Guide B defined by Eqn. (11).

Based on Eqn.(6), the sum of the normalized dumping efficiency containing all the modes of Guide A to all the modes of Guide B, i.e., the total dumping efficiency η^d_t, is thus represented by Eqn.(14) which gives

$$\eta^d_t = \frac{\sum\limits_{j,m}^{J,M} P^R_{jm} \eta^d_{jm}}{\sum\limits_{j,m}^{J,M} P^R_{jm}}$$

(14)

where η_{jm}^d is defined by Eqn. (13). With Eqn. (13) and taking $\tau_{j'm'}=100\%$, we derive the sum of the normalized dumping efficiency from a guided mode in Guide A with an even function to all the phase-matched modes in Guide B. With Eq.(14), we obtain normalized dumping efficiency summing the energy transfer from all the modes in Guide A to all the modes in Guide B (the total dumping efficiency) in Figure 3.1.3 where waveguide to waveguide separations of 5, 5.5 and 6 μm are considered. Note that the total dumping efficiency can achieve 100% at the channel length of 10 mm for S=5.0 μm. Other S values (waveguide-to-waveguide separation) have also been considered (not shown in Figure 3.1.3). The waveguide separation plays an important role in optimizing the interaction length while maintaining a large energy transfer from Guide A to Guide B. The result shown in figure 3.1.3 does not have any electric field applied across the waveguides. It is a passive coupling effect. The application of an external electric field is to eliminate the coupling and therefore achieve the intensity modulation.
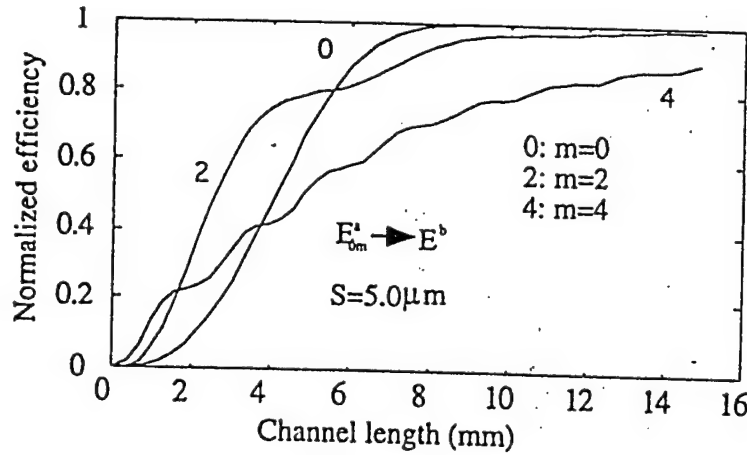
Figure 3.1.3   Total dumping efficiency from all the modes in Guide A to all the modes in Guide B without EO modulation with S= 5, 5.5 and 6.0 μm

3.1.4 Electro-optic Modulation To Eliminate the Coupling

Electro-optic modulation can change the 100% dumping efficiency from Guide A to Guide B to a lower dumping efficiency that is ~0% in an ideal case, and vice versa. Assuming the modulation voltage applied on channel A is V, we have

$$\Delta\beta_e = \frac{\pi}{\lambda}\gamma_{33}n_w^3(V / d_a) \tag{15}$$

where n_w is the waveguide index and d_a is the waveguide depth, γ_{33} is the nonlinear coefficient of the polymer material which is 18 PM/V at 632.8nm for LD-3[19]. When V is 10 volts, $\Delta\beta_e$ is about 565 in metric unit. Substituting the electro-optically modulated quantity into Eq. (14), we obtain the electro-optically modulated dumping efficiency as defined by[17,18]

$$\eta^e_{j'm',jm} = \sum_{n=0}^{N_L} \frac{k^2_{j'm',jm}}{\psi^2_e} \tau_{j'm'} \cdot \sin^2[\psi_e(n+1)\Delta L] \cdot [1 - \frac{k^2_{j'm',jm}}{\psi^2_e} \tau_{j'm'} \cdot \sin^2(\psi_e n \Delta L)] \qquad (16)$$

where

$$\psi_e = \psi_{jm,j'm'} + \Delta\beta_e / 2 \qquad (17)$$

The sum of the normalized dumping efficiency from one mode of Guide A to all the modes of Guide B under the influence of an external bias can be defined by

$$\eta^e_{jm} = \frac{\sum\limits_{j',m'}^{J',M'} P^R_{j'm'} \eta^e_{j'm',jm}}{\sum\limits_{j',m'}^{J',M'} P^R_{j'm'}} \qquad (18)$$

where $\eta^e_{j'm',jm}$ is the dumping efficiency from the (j,m)th mode of Guide A to the (j'm')th mode of Guide B in the electro-optically modulated state defined by Eqn. (16). With Eqn. (18) together with other related parameters given by the previous sections, the sum of the normalized dumping efficiency η^e_t from all the modes of Guide A to all the modes of Guide B (the total dumping efficiency) in the electro-optically modulated state can be easily derived as

$$\eta^e_t = \frac{\sum\limits_{j,m}^{J,M} P^R_{jm} \eta^e_{jm}}{\sum\limits_{j,m}^{J,M} P^R_{jm}} \qquad (19)$$

where η^e_{jm} is defined by Eqn. (18). With Eqn. (19) together with other parameters given in the previous sections, we obtain the total dumping efficiency in the electro-optically modulated. We have conducted various device configurations ranging from S=1µm to S=10µm. Figure 3.1.4 shows the modulation depth as a function of the interaction lengths with S=5, 5.5 and 6.0 µm and an applied voltage of 20 volts. With the indices of refraction as indicated, S=5µm provides us with a

11

high modulation depth of larger than 91% with an interaction length of 10 mm. With S=5.5 μm, it provides a modulation depth of larger than 98% with an interaction length of 20 mm. Figure 3.1.4 shows that the optimized design condition requires not only the correct waveguide sizes and indices but also an accurate waveguide-to-waveguide separation. Further experimental work will be conducted once the program starts.
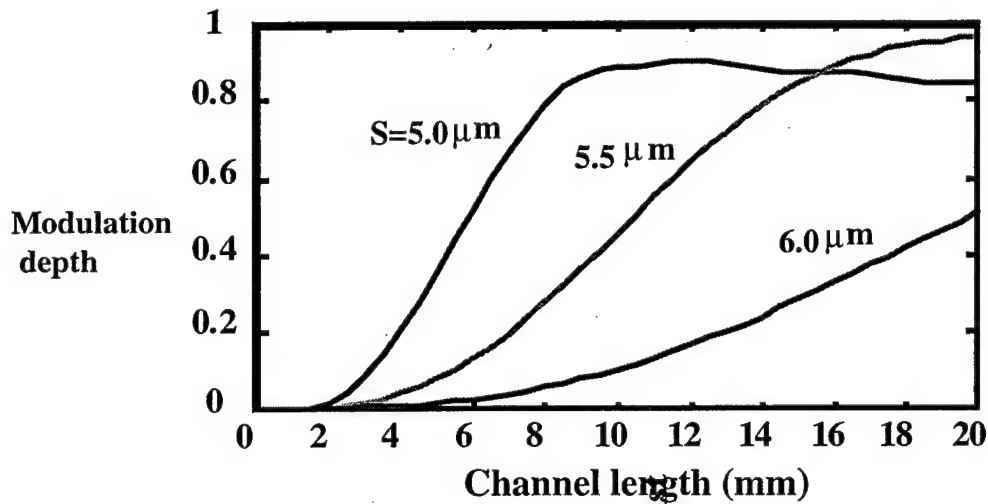
Fig. 3.1.4 EO modulation depths of modulators under a modulation voltage of 20V corresponding to different values of the separation S

3.2 Fabrications and Testing of the Coplanar Asymmetrical Unidirectional Multimode Waveguide Modulator

After theoretically analyzing the working principles of the coplanar asymmetrical unidirectional multimode waveguide modulator, we made an actual device. The 3D schematic view of the modulator is shown in Fig. 3.2.1. Fig. 3.2.2(a) shows the cross-section of the fabricated device, which contains a Si substrate, two waveguide channels (Guide A and Guide B), an upper cladding layer, a lower cladding layer, a dumping wall for unidirectional coupling, and two modulation electrodes. The top views of the real device thus fabricated is further displayed in Fig. 3.2.2(b).
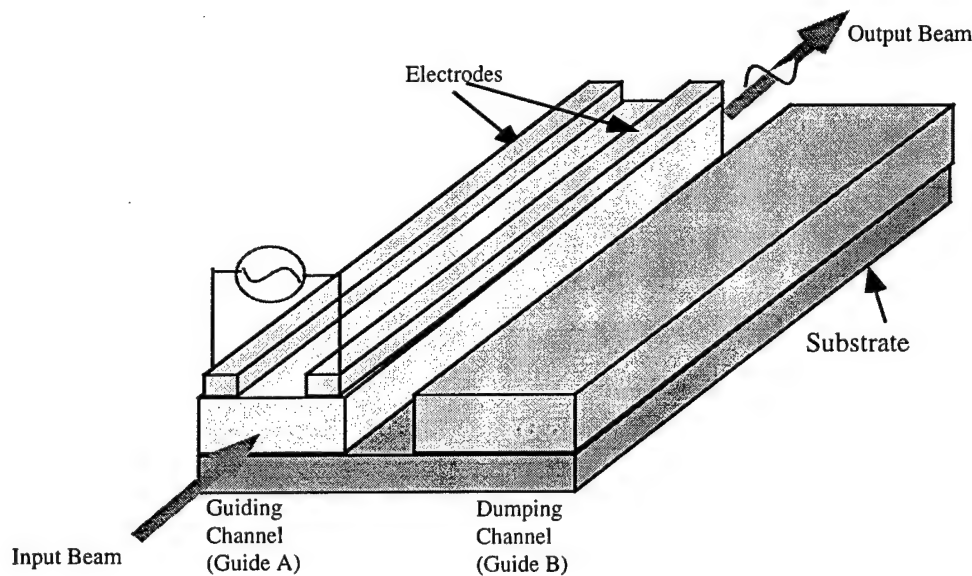
Fig. 3.2.1. Three-dimensional structure of the EO modulator based on polymer highly multi-mode waveguides.
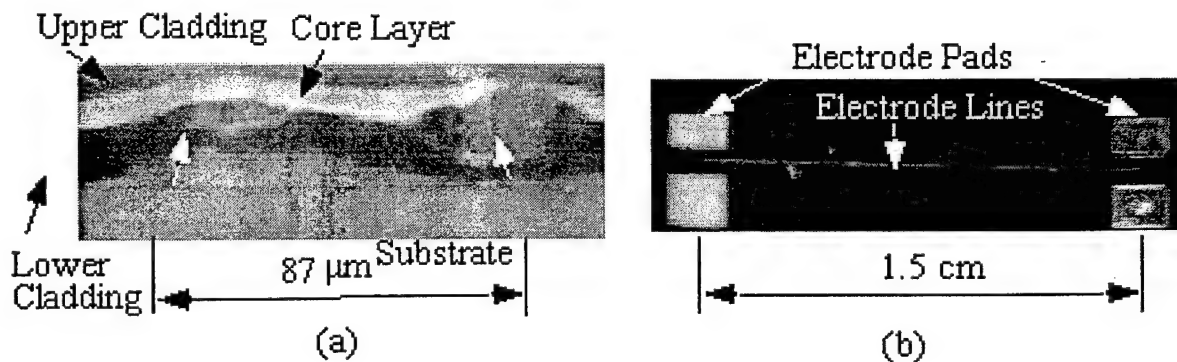
Fig. 3.2.2 the cross-section of the fabricated device
(a) cross section   (b) top view

13

The fabrication of this device mainly includes:

(1) the lower cladding layer of polyimide was spin coated on top of the Si substrate;

(2) the two deep trenches were formed using wet-etching method;

(3) a grating was made on the right-side wall as a dumping wall of the large waveguide;

(4) the waveguide layer of polymer LD-3 was spin coated on top of these two deep trenches;

(5) the two gold modulation electrodes were made with the wet etching;

The construction of the device is $d_a = d_b \approx 4.0\mu m$ and $w_a = 20\mu m$ and $w_b = 40\mu m$, respectively, and $S = 10\mu m$. In our measurements, we found that the EO coefficient of Polymer materials LD-3 was up to $\gamma33$ ~16pm/v. Fig. 3.2.3 shows the experimental results for the unidirectional EO modulator under a DC switching voltage of 30 volts. The outputs at $V = 0$ volt, and $V = 30$ volts are shown in Fig. 3.2.3 (a) and Fig. 3.2.3(b), respectively. The experimental results are obtained at wavelength $\lambda = 633\ nm$.

(a)   **(b)**
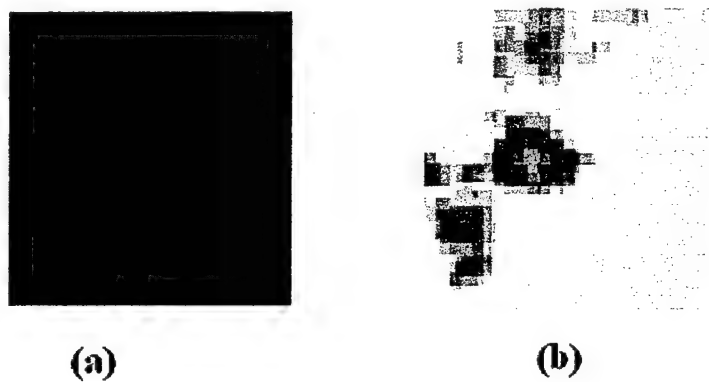
Fig. 3.2.3 Experimental results for the unidirectional EO modulator showing (a) the output optical intensity of the unmodulated state and (b) the output optical intensity of the modulated state

In summary, the introduction of the dumping effect into a highly multi-mode waveguide coupler is a new approach to improving the switching extinction of an electro-optically modulated device, which has been demonstrated theoretically. Our demonstration gives an optimized practical guided-wave switching device. The total modulation efficiency achievable is 91% for a channel length of both 10 mm and 20 mm under the modulation voltage of 20 volts. The preliminary experimental data prove that the new unidirectional EO waveguide modulator is feasible in structure and technologies.

3.3 Build Thermo-Optic Switch Based on Multi-Mode Polymeric Waveguide

To enhance the device packing density of the modulator, we improved the device design by configuring the guiding multi-mode waveguide and the dumping multi-mode waveguide vertically.

We have fabricated a polarization-insensitive thermo-optic switch based this the improved structure. This device has a packing density of 40 channels/cm in order to match the 250µm optical fiber array spacing. The simulation result shows that an extinction ratio of greater than 20dB can be achieved with a device-electrode interaction length of 30mm. The thermo-optic switch operating at wavelengths of 632.8nm and 1.3 µm has been demonstrated experimentally with extinction ratios of 21dB and 22dB, respectively. Such a device has an intrinsic wide optical bandwidth due to the large dynamic range of the phase-matching condition implied by the multi-mode waveguides. The material employed provides a switching speed of 100 µsec.

3.3.1 Device structure

The schematic and real device structures of the multi-mode thermo-optic switch are shown in Fig. 3.3.1(a) and Fig. 3.3.1(b), respectively. The device consists of a multi-mode guiding channel, a pair of heating electrodes, and a planar dumping waveguide under the guiding channel. The planar dumping layer is designed to be highly lossy (~26dB/cm) so that optic energy coupled from the guiding channel can be efficiently dumped in the dumping layer. As a result, optical energy can only be coupled from the guiding channel to the dumping layer, while the coupling from the dumping layer to the guiding channel is minimized. Thus, unidirectional coupling is achieved [26]. The electrodes were implemented to thermo-optically control the phase matching condition [27] of the coupling between the guiding channel and the dumping layer. Because there is only one channel per switch in this structure, the device packing density (number of switches per unit area) can be twice that of devices with a co-planar configuration [26], where guiding and dumpling channels are implemented in the same layer.

(a) schematic view of the device structure   (b) SEM view of the device structure

① heating electrodes

② guiding channel

③ dumping planar waveguide

④ substrate
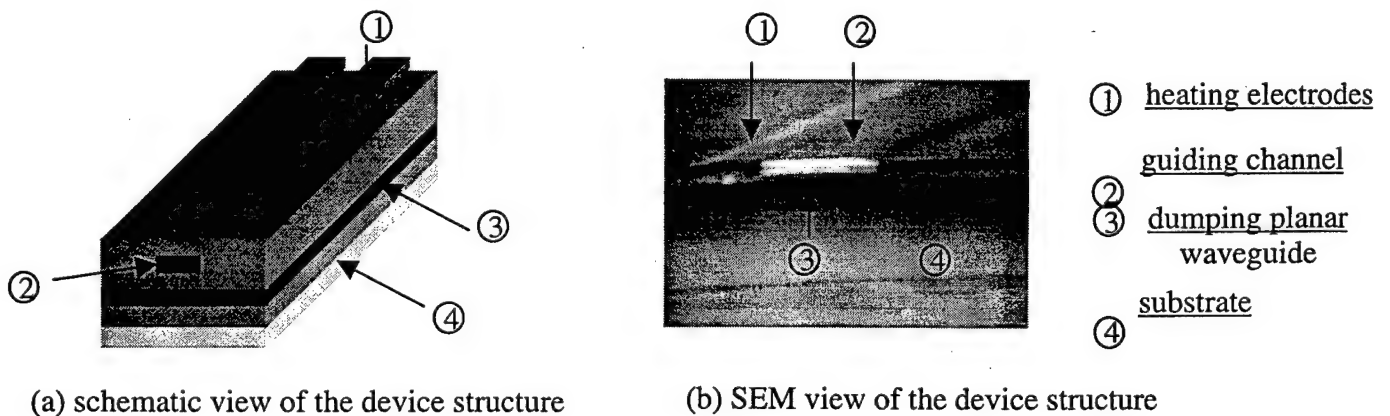
Fig.3.3.1 Structure of the unidirectional thermo-optical switch.

3.3.2 Device Simulation Using BeamProp®

To control the phase matching condition thermo-optically, a pair of heating electrodes was implemented on top of the guiding channel. By applying current induced heat through the electrodes, the temperature difference between the guiding channel and the other areas of the device (ΔT) can be changed continuously. Beam propagation software (BeamProp®) was used to simulate the device operations at two switching states ($\Delta T = 0$ °C and 30 °C) at 632.8nm and 1.3μm respectively. The simulation result of 632.8nm is shown in Fig.3.3.2. The output optical energy of the guiding channel was high (Fig. 3.3.2 (a)) when ΔT was 0 °C. When ΔT was 30 °C, the light in the multi-mode guiding channel was coupled to the dumping layer, which was a highly multi-mode planar waveguide. The output optical energy of the guiding channel became low (Fig. 3.3.2 (b)), satisfying the phase match condition.

signal in the guiding channel

signal in the dumping planar waveguide

(a) $\Delta T = 0$°C

(b) $\Delta T = 30$°C
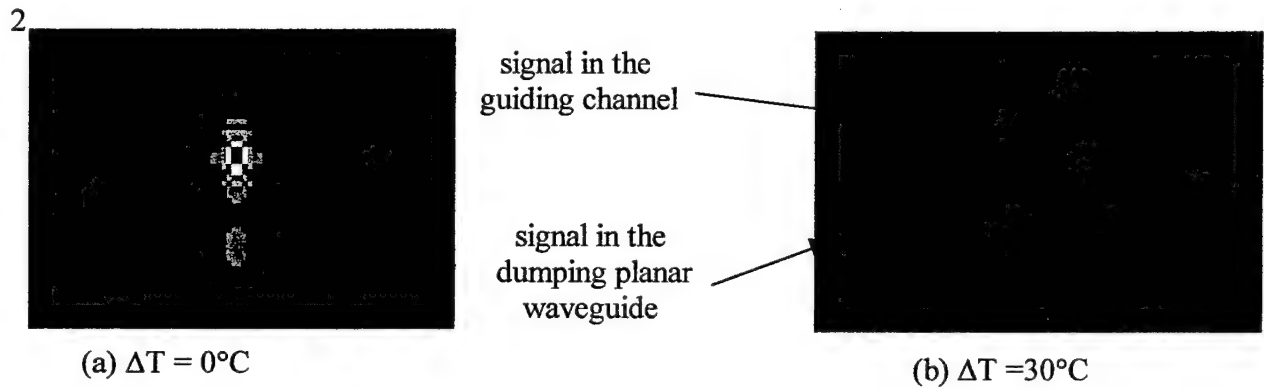
Fig.3.3.2 Simulation result of near-filed output pattern of the thermo-optical switch.

(a) when the temperature difference ΔT was 0°C.
(b) when the temperature difference ΔT was 30°C.

3.3.3 Dumping efficiency calculation and simulation

The extinction ratio between the on- and off -state is an important parameter in the thermo-optic switch. We use the unidirectional coupling mechanism to achieve a high extinction ratio between the on- and off- states. To determine how the dumping layer improves unidirectional dumping efficiency, we simulated the dumping efficiency from the guiding channel to the planar dumping layer based on the unidirectional coupling mechanism [26]. Fig. 3.3.3 shows the simulation result of the sum of the dumping efficiencies from all modes of the guiding channel to all modes of the dumping layer. Note that dumping efficiency of more than 20dB can be achieved with the channel length of 30mm. This shows that the planar dumping layer can effectively improve the dumping efficiency.
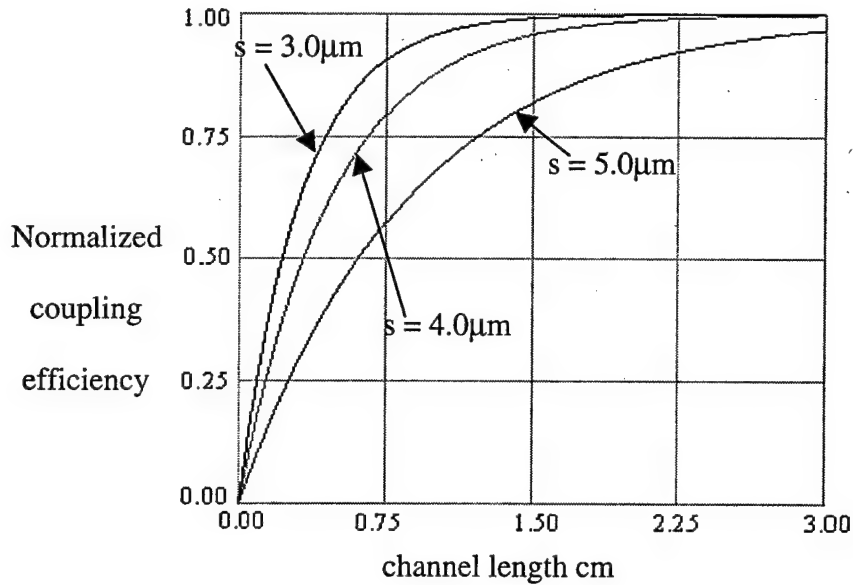
Fig. 3.3.3 Normalized coupling efficiency as function of channel length.
upper -- s = 3.0 μm, middle s = 4.0 μm lower -- s = 5.0 μm;
where s is the separation layer thickness.

3.3.4 Device Fabrications

3.3.4.1 Polymer – Photo lime gel

The device we built is based on the photo lime gel guest/host polymer. Gelatin has extraordinary chemical and physical properties such as two-dimensional network and heat or UV curing [19]. These features of gelatin can be used to develop a graded-index profile waveguide through wet processing, swelling, and dehydration [19]. Furthermore, high quality optical waveguides with loss less than 0.1dB/cm [16] can be made using gelatin polymer. Gelatin polymer is also used as the holographic recording material, dichromate gelatin (DCG) [19].

The optical thin film was formed by mixing gelatin and chlorophenol-red solution (CR), and spinning the solution on top of a silicon wafer (with a buffer layer of Masterbond UV 15). By changing Gelatin to water ratio and spin coating speed, we can get optical thin films of different thickness that can be used both for single and multi-mode waveguide channels. The procedure of making gelatin / chlorophenol-red films is showed in Fig. 3.3.4:
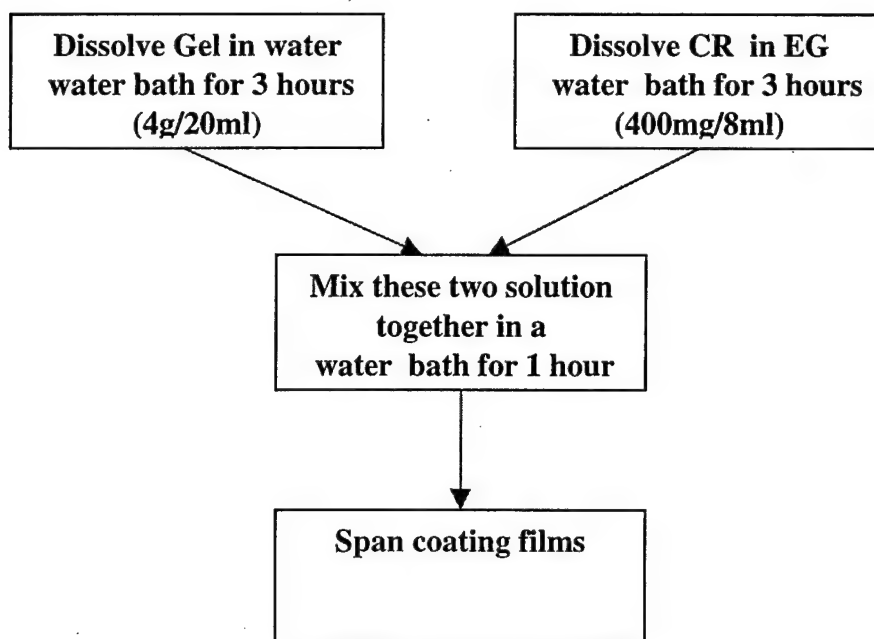
Fig. 3.3.4 Procedure for making optical thin film

The refractive index of the film can be adjusted by changing the percentage of CR. The relationship between the CR concentration and the film refractive index is shown in Fig. 3.3.5.
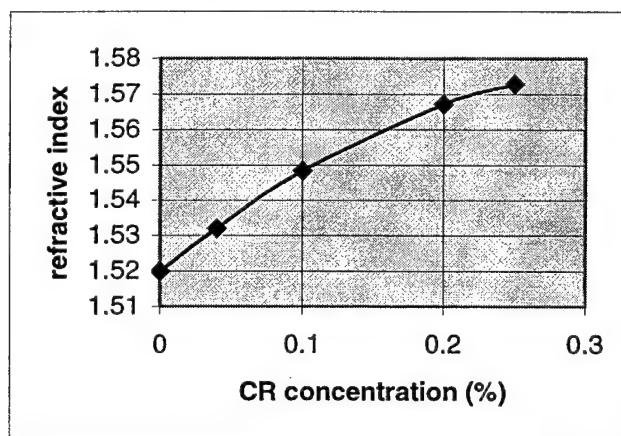
Fig. 3.3.5 Refractive index as function of CR concentration

For a NLO film, the greater the CR concentration, the larger the nonlinearity. Therefore, because of this direct relationship, more CR concentration is needed. However, as we can see from Fig. 3.3.5, the refractive index also increases when CR concentration increases. Since the refractive index of the cladding layer (UV 15) is 1.52 at the wavelength of 632.8nm, if the refractive index of Gelatin/CR is

too high, the guiding waveguide and the dumping waveguide must be brought closer, which will make fabricating the device more difficult. Another difficulty arises because more CR concentration will increase the loss of the waveguide due to the CR absorption of light. In our experiment, we choose the concentration (%CR) to be 10%. The resulting refractive index is 1.547.

Once the film is formed, it can be transformed into a highly cross-linked polymer using heat or UV curing. To examine the effect of UV curing on the refractive indices change, we measured the relation between the refractive indices of TE mode and TM mode and UV exposure dosage (J/cm²). The refractive indices of the film increase when the film is subjected to UV exposure. When the UV exposure dosage reached a certain level, the refractive indices of TE mode and TM mode stabilized, which indicated that UV exposure in the device processing does not significantly change the film properties. Fig. 3.3.6 shows the refractive index change as a function of UV exposure energy.
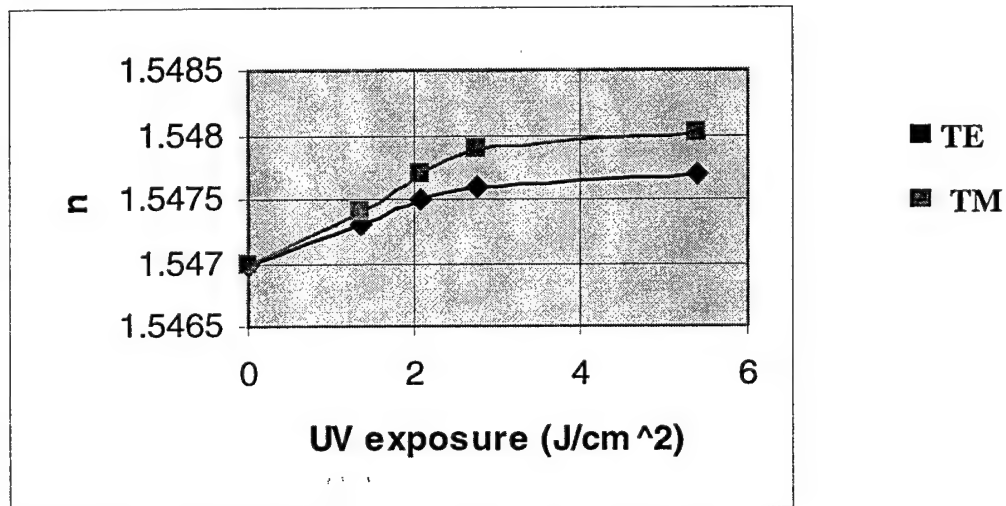
Fig. 3.3.6 Refractive index change as a function of UV exposure

3.3.4.2 Choice of the Cladding layer

The characteristics of devices rely on both the waveguide materials and the cladding materials [17], [18]. The cladding layer must have: (1) a lower refractive index than the guiding layer; (2) thermal stability; (3) optical transparency. For thermo-optic switch devices, the cladding layer must have good thermal conductivity and less thermal coefficient than the guiding layer. Furthermore, the cladding layer thickness also affects the switch voltage and the loss of the guiding layer [20].

3.3.4.2(a) The cladding layer material – Master Bond UV15®

Master Bond UV15 is a new one-component, high-strength UV curable resin-based polymer. When it is exposed to a source of UV light, Master Bond UV 15 produces durable, strong, chemically resistant coatings with excellent electrical and optical properties. Some of its properties are listed in Table 3.3.1.

Table 3.3.1 Properties of UV 15

Water resistance	Acetone resistance	Refractive index (632.8nm)	Dielectric constant (1MHz, 25°C)	Volume Resistivity (megohm-cm)
Excellent	Excellent	1.519	2.96	1.6 G

3.3.4.2(b) Calculation of cladding layer thickness

The thickness of the cladding layer is an important parameter for a thermo-optic switch. Less cladding thickness results in lower switching voltage. However, with a thinner cladding layer, silicon substrate absorbs part of the energy of guiding modes through the evanescent tail of the guided modes. This absorption causes loss of the guided modes. The loss becomes more serious for the higher-order modes because their evanescent tails penetrate farther than those of lower-order modes. The thinner the buffer layer, the greater the loss is. Fig. 3.3.7 shows the calculation of the loss of the guiding layer as the function of cladding layer thickness for TE10 mode and TE11 mode. As we can see from Fig. 3.3.7, the loss of both TE10 and TE11 modes decreases as the cladding layer thickness increases. When the cladding layer thickness reaches 4.0μm, the loss of TE10 mode is almost 0. Based on this calculation, we choose a cladding thickness of 4.0μm.

3.3.4.3 Fabrication Procedure

We follow the standard VLSI fabrication procedure, which makes the fabrication of the device compatible with that of microelectronic devices.

3.3.4.3(a) Substrate preparation

The substrate of the thermo-optic switch can be glass, silicon wafer or a PC board. For reasons of compatibility with standard microelectronic devices, we chose a P- type silicon wafer as the substrate. The substrate was cleaned using first Acetone for 3 minutes, and then ethanol for 3 minutes. After that, DI water was used to wash away the remaining chemicals. After cleaning, the silicon wafer was baked at 160°C for one hour to dehydrate it, then was spin-coated with A/B 600

promoter to improve the adhesion of the wafer with the bottom cladding layer. A UV 15 bottom cladding layer was then spin-coated on the wafer, at a speed of 5000rpm, resulting in a bottom cladding layer with a thickness of 4.1μm.
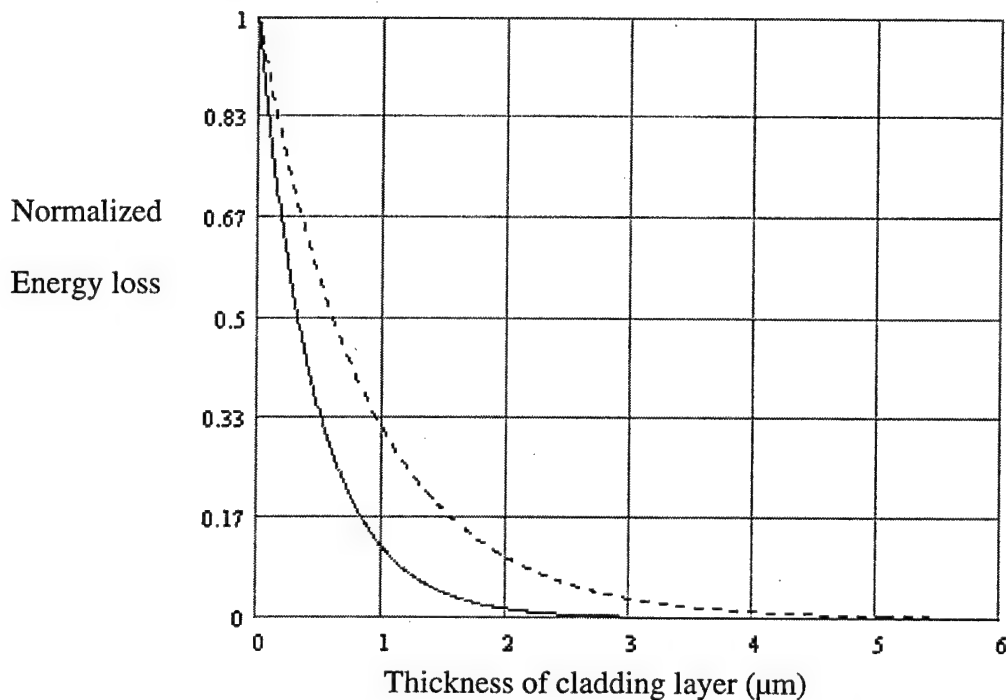
Fig. 3.3.7 Energy loss vs. cladding layer thickness

3.3.4.3(b) Making Photolime gel films

The optical thin film was formed by first mixing gelatin and chlorophenol-red solution, and then spin-coating the solution on the silicon wafer. The CR to Gelatin ratio is 1:5 (20% weight concentration), The spin coating speed is 430rpm. The thickness of the film is 4.2μm. The refractive index is 1.547.

3.3.4.3(c) Defining of multi-mode waveguide channels

The fabrication of the multi-mode waveguide channels followed the conventional lithography technique used in VLSI fabrication. The multi-mode channel waveguide of 20.0 μm × 4.2 μm was defined using lithography and then reactive ion etching (RIE) techniques. The thickness of guiding, dumping and cladding layers were 4.2μm, 4.4μm and 4.1μm, respectively.

3.3.4.3(d) Forming of top cladding

21

Master Bond UV15® was used as both the top cladding and the bottom cladding. The refractive indices of UV15® are 1.52 at 6328nm and 1.49 at 1.3μm.

3.3.4.3(e) Forming of top electrodes

The top heating electrodes were formed by a conventional lift-off method, shown in Fig. 3.3.8. The sample was first spin-coated with a thin layer of photo resist AZ5209 with a thickness of 1μm. The sample was then patterned using the lithography method. A thin layer of Cr and Au was then thermally deposited on the sample. The thickness of the Cr layer was 170Å, and the thickness of Au layer was 1500 Å. The thin Cr layer was used to improve the adhesion of the polymer layer and the Au layer. The sample was then put into acetone for 3 minutes to strip away the remaining metal layer.
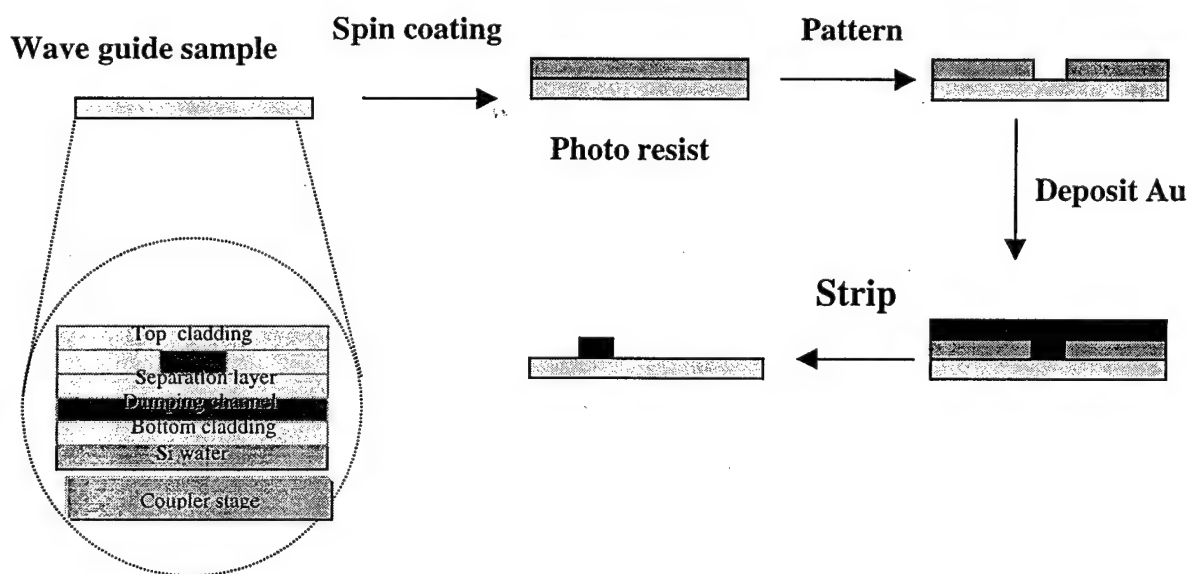
Fig.3.3.8 Procedure for making top electrodes

The alignment of the top electrodes with respect to the channel waveguide is critical to the process of device fabrication. A microscopic view of the alignment of the top electrodes and the channel waveguide is shown in Fig. 3.3.9. The length of the electrodes and that of the total device were 3.0 cm and 3.6 cm respectively. The resistance of the electrodes was measured to be 78 Ω.

3.3.5. Experiment results

The schematic view of the experiment setup is shown in Fig. 1.10. A photograph of the coupling stage is shown in Fig. 3.3.11.
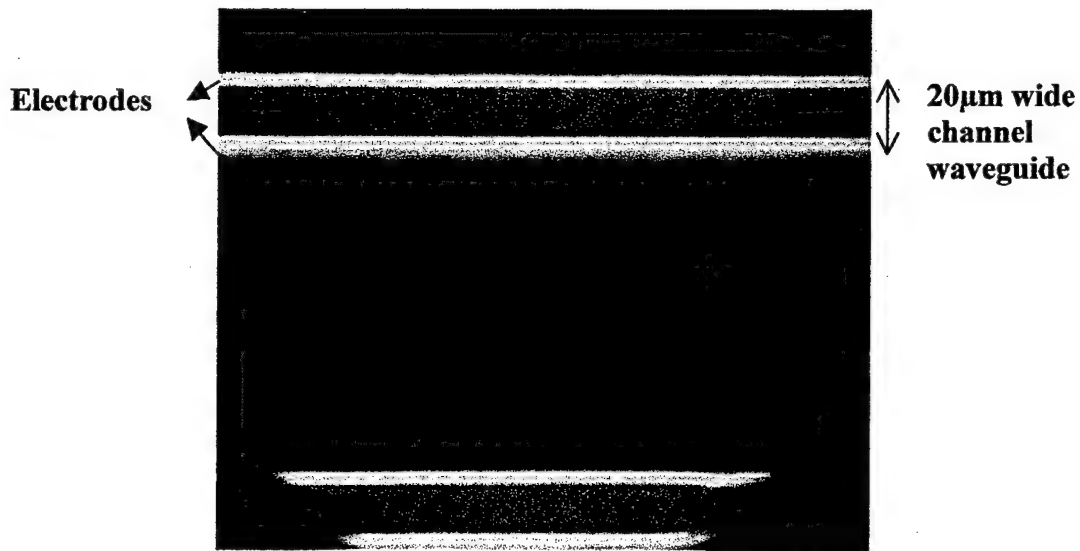
Fig. 3.3.9 The alignment of top electrodes and channel waveguide
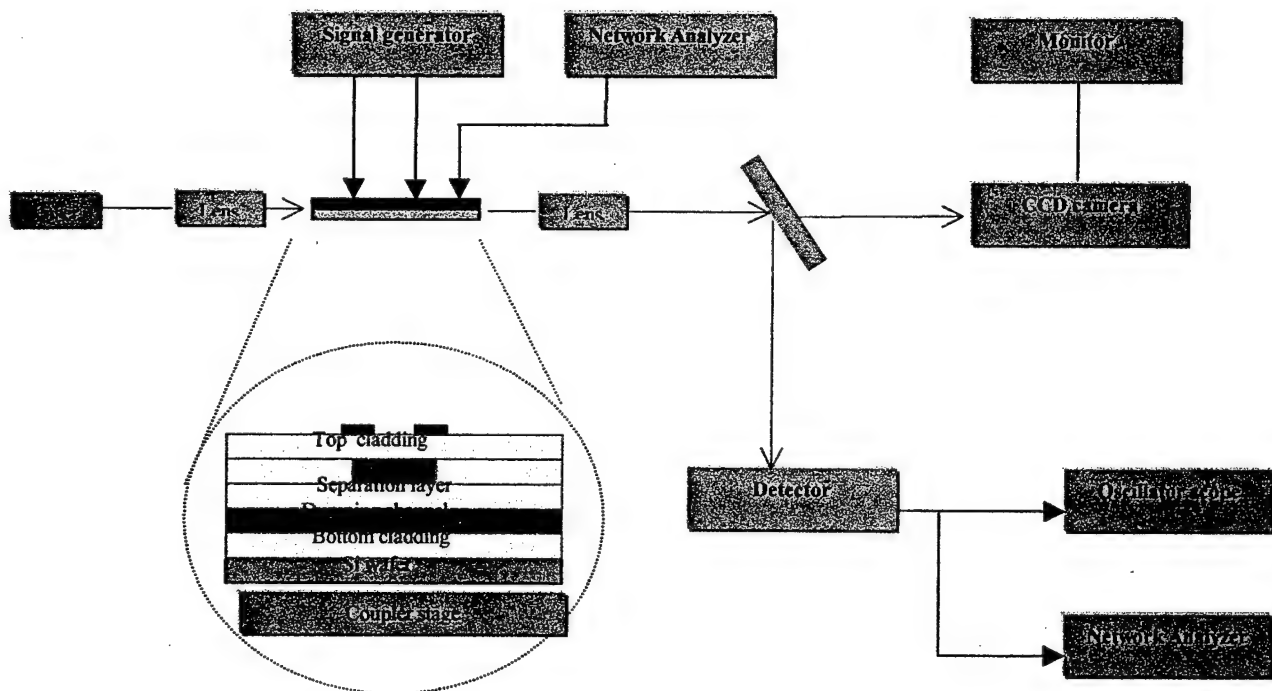
Fig. 3.3.10 schematic view of experiment setup

A 632.8nm wavelength laser beam was endfire coupled into the device through a 40X objective lens. The output light was focused through another 40X objective lens and then imaged onto a screen. An IR camera was used to obtain the near field real-time image, which was then collected by a computer and analyzed by a Spiricon™ beam analyzer. An optimized 5V voltage was applied to the electrode, corresponding to a heating current of 62mA. Unlike conventional single mode devices which are highly wavelength sensitive, the device reported herein is an intrinsically wide-band device due to the large dynamic range of the phase match conditions [26,29].
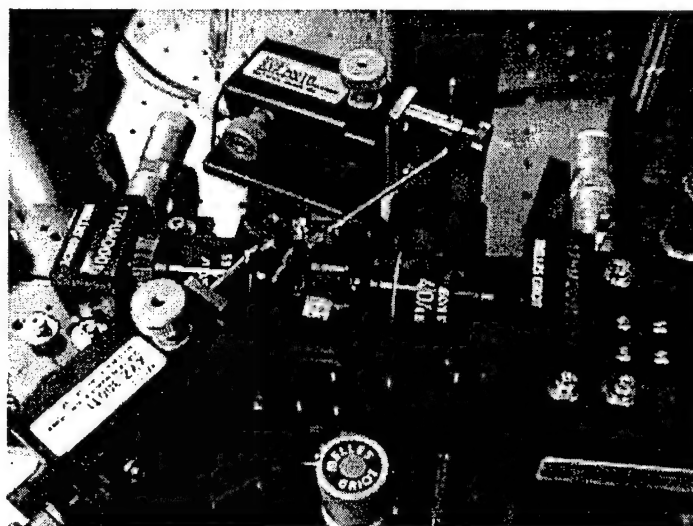
A: Test Arms; **B, C**: objective lens; **D**: device under test

Fig. 3.3.11 coupling stage

Experimental results of 632.8nm and 1.3μm are reported in this section. For the case of 632.8nm, Figure 3.3.12 shows the two-dimensional (2D) and three-dimensional (3D) view of near field output patterns. With no heating current, the output of the guiding channel was high (Fig. 3.3.12 (a), 3.3.12 (c)), i.e., the phase matching conditions were not satisfied. The light in the guiding channel was dumped to the dumping layer and the output of the guiding channel was low (Fig. 3.3.12 (b), 3.3.12 (d)) when a heating current of 62mA was applied. The phase matching conditions were induced and a high extinction ration of -21dB was observed.

For observation of the switching operation at the wavelength of 1.3μm, a 1.3μm wavelength laser beam was coupled into the same device through the same experimental setup using the same switching voltage. The three-dimensional (3D) view of near field output patterns at 1.3μm is shown in Figure 3.3.13. With no heating current, the output of the guiding channel was high (Fig.

At a heating current of 62mA,the light in the guiding channel was dumped to the dumping layer and the output of the guiding channel was low (Fig. 3.3.13 (b)). The extinction ratio was measured to be -22dB, which is almost the same as that of 632.8nm operation. Note that both 632.8nm and 1.3μm laser beams were randomly polarized. Unlike the EO effect, which is polarization-sensitive, the TO switching device reported herein is polarization-insensitive.

signal in the guiding channel

signal in the dumping planar waveguide

(a) 0mA heating current

(b) 62mA heating current

signal in the guiding channel

signal in the dumping planar waveguide

(c) 0mA heating current

(d) 62mA heating current
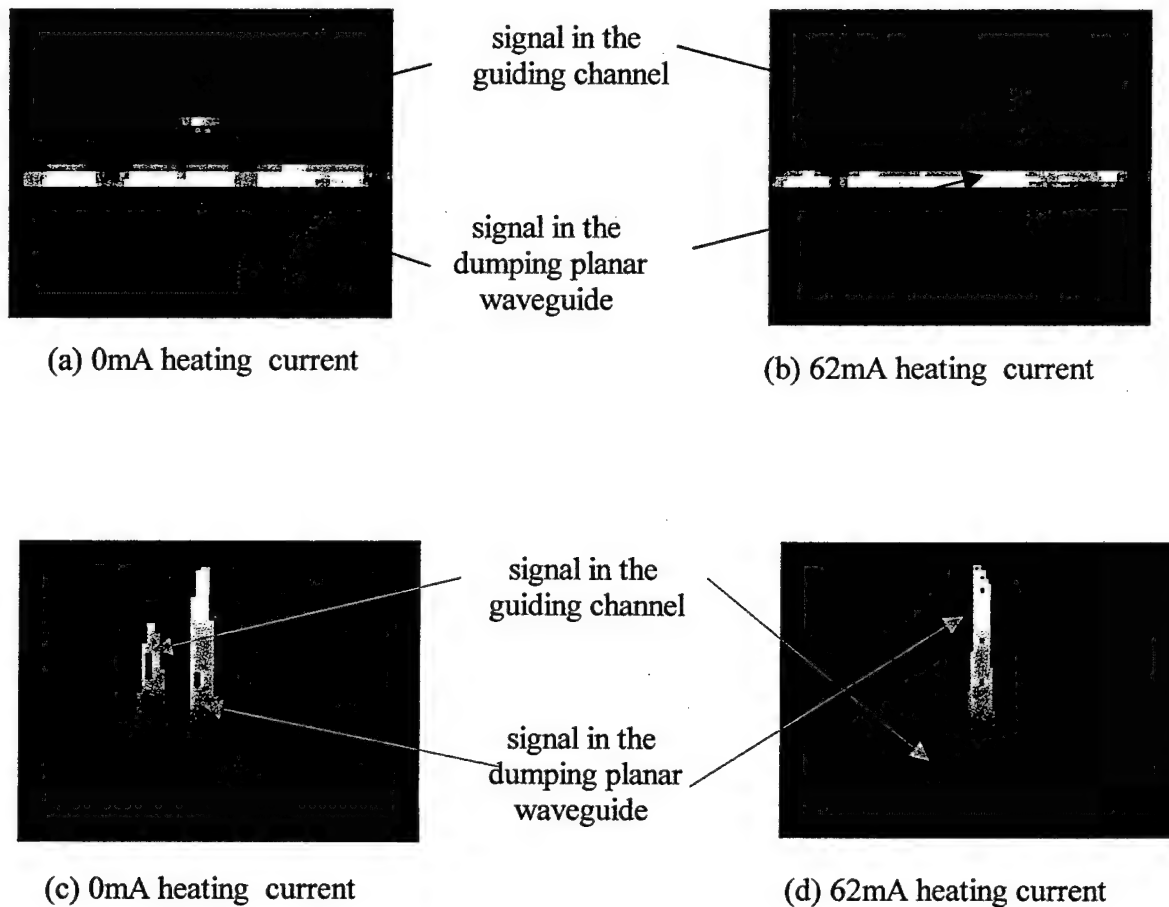
Fig. 3.3.12 Experiment results of the near filed output patterns of the thermo-optical switch at 633nm. (a),(b)2-D view, (c),(d) 3-D view.
   (a) (c) without heating current.
   (b) (d) with heating current of 62mA.

signal in the
guiding channel

signal in the
dumping planar
waveguide
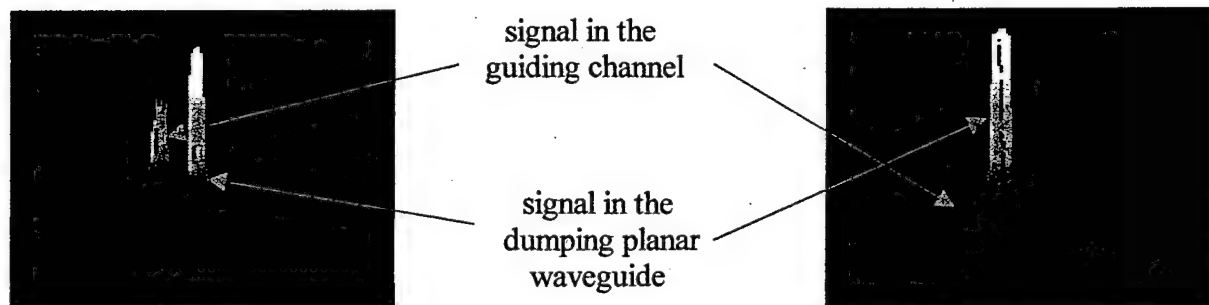
Fig. 3.3.13 Experiment results of the 3D near filed output patterns of the thermo-optical switch at 1.3μm.   (a) without heating current.   (b) with heating current of 62mA.

In summary, we have made a novel multi-mode thermo-optic polymeric switch, covering an ultra-large optical bandwidth. Due to the vertical layout of the dumping planar waveguide, the device has a device packing density of 40 channels/cm to match 250μm fiber array spacing. Dumping efficiency of greater than 20dB was achieved with the interaction length of 30mm. Thermo-optic switching for randomly polarized light at wavelengths of 632.8nm and 1.3μm has been observed experimentally using the same device.

3.4 Contact poling of the nonlinear optical film (PMMA/DR1)

Poling of nonlinear optical (NLO) film is an important step in building an electro-optic modulator on polymer. There are two kinds of poling methods: (1) Corona Poling and (2) Contact Poling. The schematic views of contact poling and corona poling apparatus are shown in Fig. 3.4.1. During corona poling, many defects are created at the top surface of the film. These defects introduce a large amount of loss into waveguides. In the worst case, light can not even be guided through waveguides. Contact poling has such advantages as less poling voltage and more accurate poling voltage control. Fig 3.4.2 shows the film after corona poling and contact poling. It is obvious that contact poling introduce less surface defects than corona poling. However, impurities and defects in the samples will result in short circuits and therefore destroy the samples during the contact poling. For this reason, we have to be very vigilant about defects introduced in the fabrication of devices.

Fig. 3.4.1(a)   **Fig. 3.4.1 (b)**
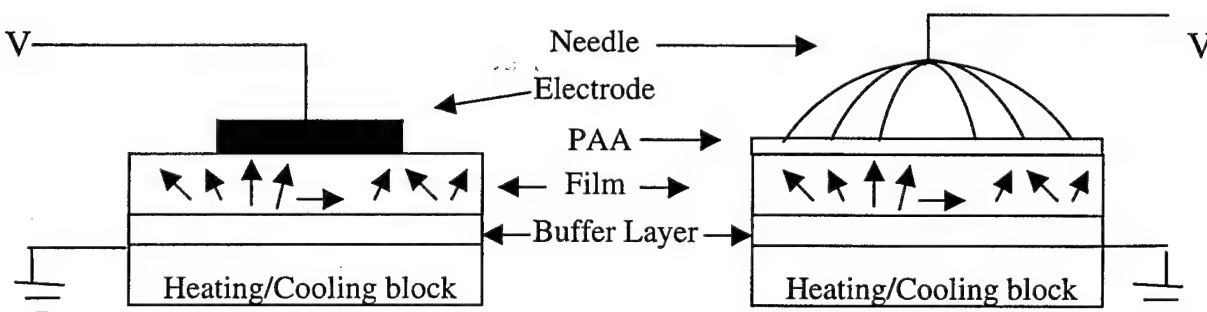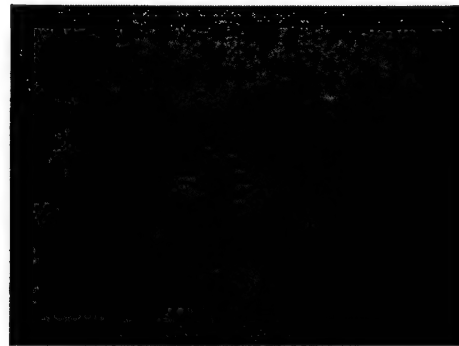
Fig. 3.4.1 Poling apparatus (a) Contact Poling; (b) Corona Poling

(a) film surface after corona poling   (b)film surface after corona poling

Fig. 3.4.2 Corona Poling vs. Contact Poling;

3.4.1. EO Polymer – PMMA/DR1

Although photo lime gel guest/host NLO polymer has several advantages such as low optical attenuation (0.1/dB/cm) and high nonlinearity [19], it is difficult to process because it dissolves in water. Further more, the long-term stability is poor because it absorbs moisture in the air. Therefore, we changed the NLO polymer to disperse red 1(DR1) side chained poly(methyl methacrylate) (PMMA/DR1, a polymer from IBM Almaden Research Center). Unlike the photo lime gel guest/host NLO polymer, PMMA/DR1 is not water-soluble. Thus creates an advantage in the device processing. Because one end of the DR1 chromophore is covalently attached to the PMMA backbone, it has high nonlinearity. Some EO parameters of PMMA/DR1 are shown in Table 2. Many waveguide devices based on PMMA/DR1 have been developed [30-31].

The EO effect in polymer originates from the alignment of chromophores that cause the non-central symmetry. This kind of angular alignment of chromophores can be induced by the poling process[32] which is discussed in detail in the following section.

3.4.2 Sample preparation and poling

To prepare PMMA/DR1 solution, 0.2g PMMA/DR1 is first dissolved in 1 ml cyclopentanone, then filtered with a 0.2μm filter. To prepare samples for contact poling, a thin bottom electrode layer of Au (1100 Å) was first thermally deposited on a substrate, which was then spin-coated with a thin layer A/B 600 promoter (otherwise the film may peel off during device processing), and then spin-coated with a 3μm buffer layer (MasterBond UV15®). The PMMA/DR1 solution was next spin-coated on the prepared substrate at a spin coating speed of 400rpm. After that, the samples were baked at 90°C with Nitrogen purging for two hours. The thickness of PMMA/DR1 polymer film is 5.1μm. The refractive index of the PMMA/DR1 polymer is 1.59 at 632.8nm and 1.57 at 1.3μm.

3.4.2(a) Break-down voltage measurement

Since the samples are subjected to high voltages during contact poling, an applied poling voltage higher than the break down voltage will destroy the films. Therefore, break-down voltage is an important factor during the contact poling process. The break-down voltage is measured by measuring the current of the poling circuit at the EO polymer's glass transition temperature (Tg) [32]. The Tg for PMMA/DR1 is 125°C [32]. The I-V curve is shown in Fig.3.4.3. There are three regions in the I-V curve, region I, II and III. In region I, the current I, which is very small (almost 0 μA), is independent of the poling voltage increase, which indicates that the circuit is open and the dipoles in the film are randomly polarized. In region II, the current increases as the poling voltage increases. However, the I –V relation is nonlinear, which shows that the dipoles in the film were changing from randomly polarized status to a status that is somewhat aligned. In region III, the

current increases sharply when the poling voltage increases. In this region, the film was broken down by the poling voltage. From the I-V curve, we can measure the break-down voltage of PMMA/DR1 at the Tg to be 900 (V).
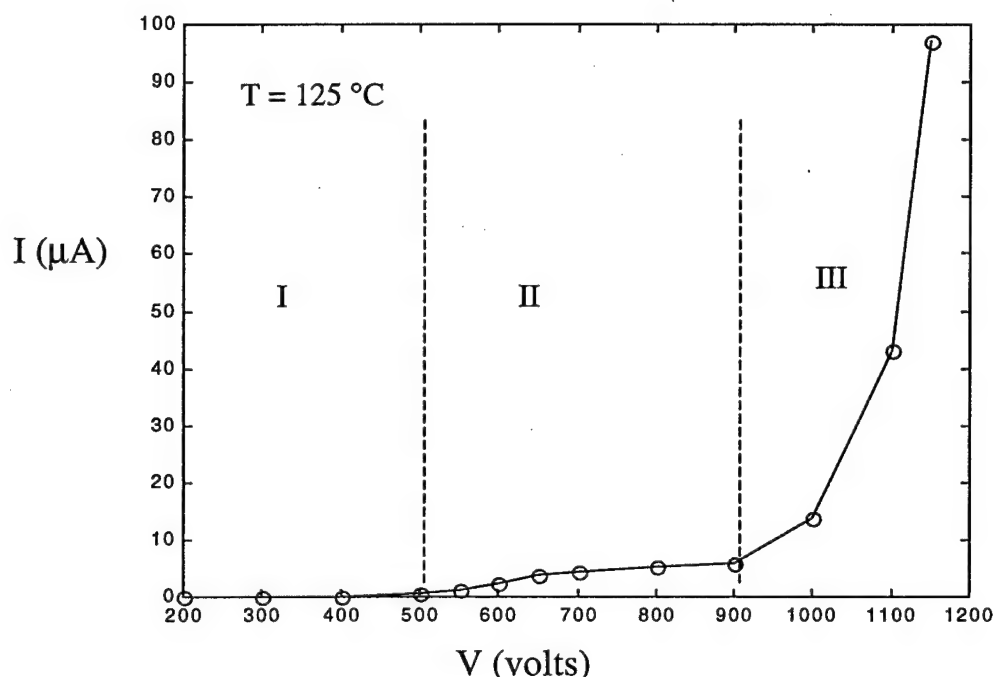
Fig. 3.4.3 I-V curve for film break-down voltage measurement

After obtaining the break-down voltage for PMMA/DR1 film at the Tg, we poled more PMMA/DR1 samples at the poling voltage of 800(v), which was slightly less than the break down voltage. After it was poled, the film was quickly cooled while keeping the poling voltage 800(v) to freeze the dipoles aligned in the films.

3.4.2(b) Refractive indices change after corona poling

After corona poling, we measured the refractive indices of the TE modes and TM modes of the poled film. The wavelength of the measurement is 632.8nm, as shown in Table 3.4.1. As we can see from that table, the refractive index of TE mode decreases after poling and the refractive index of TM mode increases. The refractive index difference between TE and TM mode is approximately $\Delta n \sim 0.007$. This poled induced birefringence is very a key factor in the phase modulator.

Table 3.4.1

	Before poling	After poling
n (TE)	1.594	1.591
n (TM)	1.594	1.598

3.4.2(c) Electrooptic coefficient measurement

There are many different ways to measure the electrooptic coefficient [19]. We used a simple and direct method to determine the electrooptic coefficient by measuring the birefringence induced by contact poling electric filed. The schematic view of the experimental setup is shown in Fig. 3.4.4.

A: polarizer, B: waveguide and electrodes
C: analyzer, D: detector
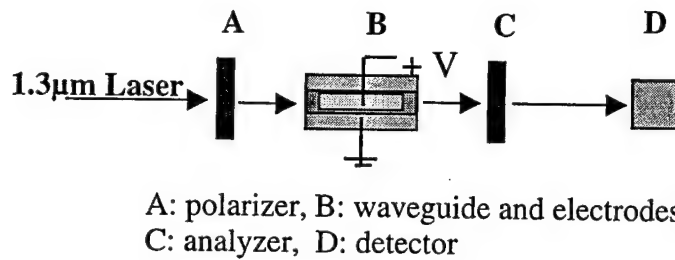
Fig. 3.4.4 schematic view of the experimental setup of measuring EO coefficient

As shown in Fig. 3.4.4, 1.3μm Laser was 45 degree polarized with regard to the vertical direction by the polarizer A. After passing through the film with a waveguide and a top electrode B, the polarization plane rotation was detected by the analyzer C. We measured the ploarization plane rotations under two different conditions: (1) V= 0(V), (2) V= 100V. By measuring the plane rotations difference between these two different states, we can estimate the γ_{33} of the poled film. Table 3.4.2 shows the experimental result.

Table 3.4.2 Polarization plane rotations under different voltages

Voltage (V)	0	100
polarization plane rotations (degree)	15.4	60.8

$$\Delta\beta = n_e{}^3\gamma_{33}\alpha V/d \qquad (20)$$

where β is the propagation constant, n_e is the effective refractive index, α is the overlap integral between the applied electrical field and the optical field ($0<\alpha<1$).

$$\Delta\beta = (2\pi/\lambda)(n_{TE} - n_{TM})L \qquad (21)$$

where λ is the wavelength of the Laser, n_{TE} and n_{TM} is the effective refractive indices of the TE mode and the TM mode of the waveguide, L is the electrode length. Based on the experimental result, the γ_{33} is estimated to be 12pm/V.

3.5 Channel Array Multi-mode Electro-optical Modulator with Guiding Channels and Dumping Layer Vertically Configured

In order to increase the device packing density, we build a electrooptic modulator by configuring the guiding channel and dumping channel vertically. Instead of using a dumpling channel, a planar waveguide is used as the dumping layer. The Dumping planar waveguide is also designed to be lossy (~-26db/cm) as in the thermo-optic switch. Light coupled from the guiding channel is refracted in all the directions and is dumped. Therefore a unidirectional mechanism is achieved. By exploring this configuration, the device packing density can be increased by a factor of two.

3.5.1 Device Structure

The schematic device structure is shown in Fig. 3.5.1. The top view of the real device is shown in Fig. 3.5.2. Fig. 3.5.3 shows the cross section of the real device. As shown in these figures, the electro-optic modulator consists of a dumpling planar waveguide (with loss coefficient of ~-26dB/cm), multi-mode guiding waveguides, and modulating electrodes. The modulating electrodes were used to adjust the effective refractive indices of the guiding multi-mode waveguide to match those of the dumping planar waveguide.

3.5.2 Device Fabrication

The device fabrication procedure follows the standard VLSI fabrication procedures that are using in microelectronic industry. There were eight steps in the device fabrication:

(1) Substrate preparation

Because P-type Si wafer is widely using in microelectronics industry, We chose a P- type silicon wafer as the substrate of the device. The substrate was first cleaned using first Acetone for 3 minutes, and then ethanol for 3 minutes. After that, DI water was used to wash away the remaining chemicals. After cleaning, the silicon wafer was baked at 160°C for one hour to dehydrate it. A 110Å thick Cr layer was thermal deposited on to the surface of the Si substrate. This layer was used to improve the adhesion between the Si substrate and subsequent layer. A thin Au layer was then thermal deposited on to the sample. The thickness of the Au layer was measured to be 1100Å, This
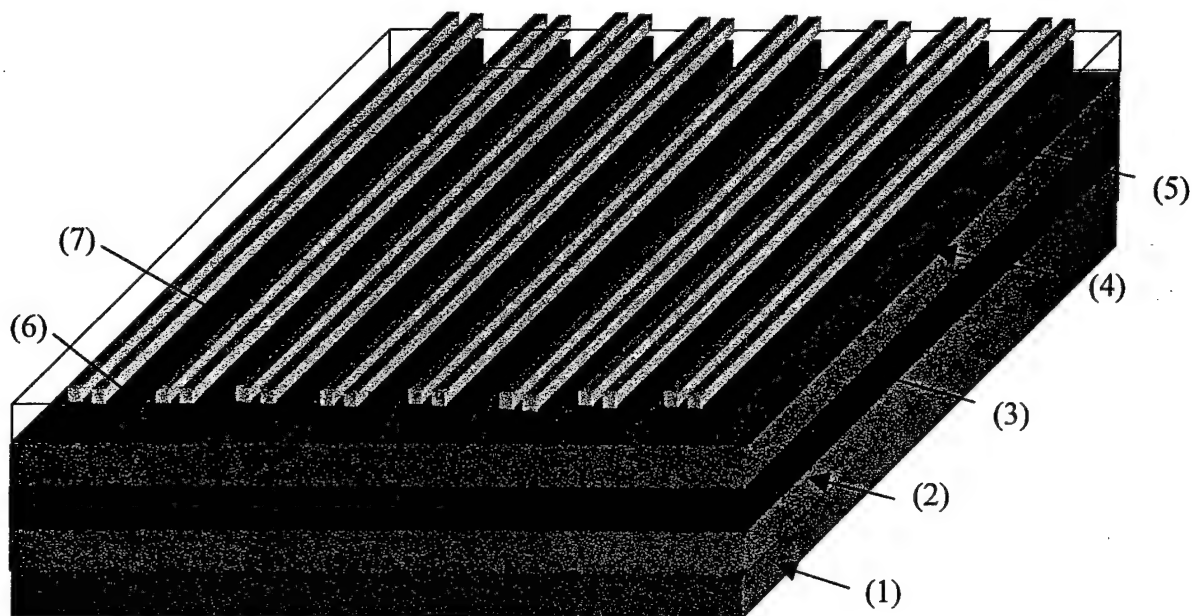
Fig. 3.5.1 Layout of multi-mode channel array Modulator

(1) substrate   **(2) bottom**   **(3) dumping layer**
(4) buffer layer   **(5) top**   **(6) multi-mode channel**
(7) modulating electrodes
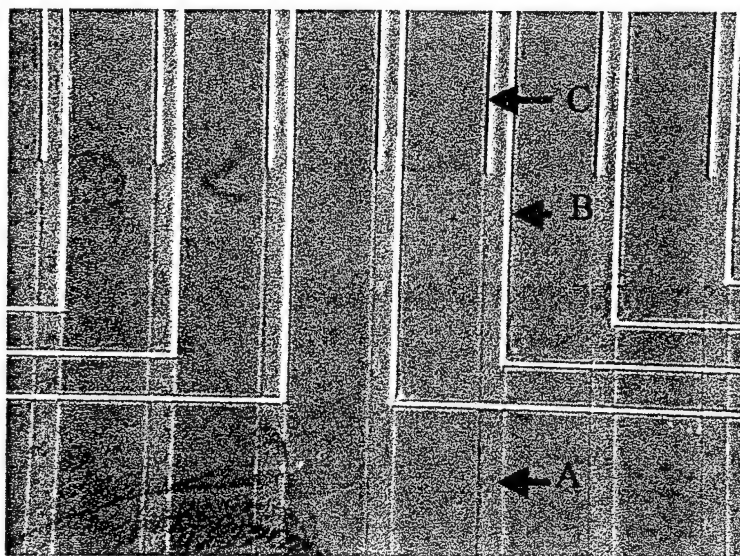
Fig. 3.5.2 Top view of multi-mode channel array Modulator

A: 50µM   **B : Modulating electrodes   C : top electrodes**

2.2μm

3.5μm

Buffer layer   Dumping layer   Bottom cladding

Si substrate
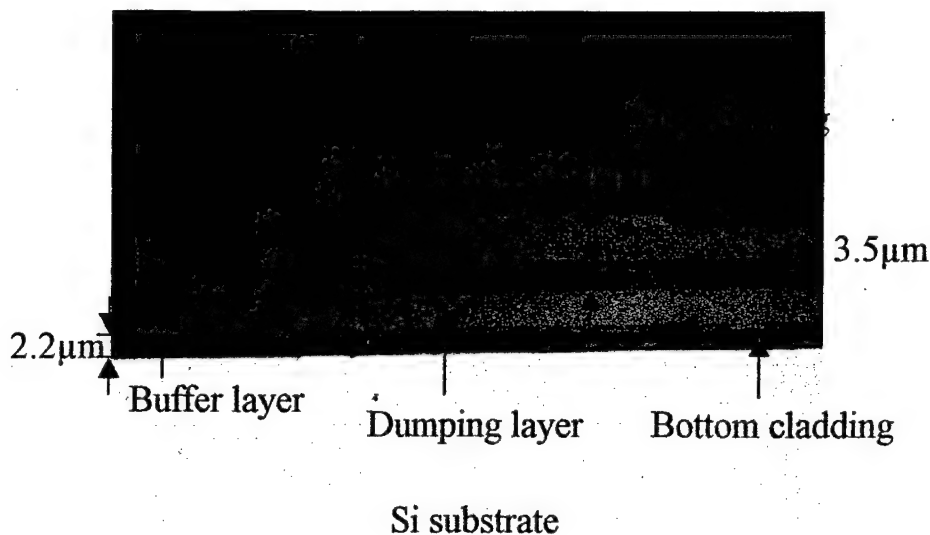
Fig. 3.5.3 Cross section of multi-mode channel array

Au layer was used as the bottom electrode during the contact poling. Then an Armoco U9020 bottom cladding layer was spin-coated on to the sample. The spin-coating speed is 3500rpm, which resulted in a bottom cladding thickness of 2.2μm. The refractive index of U9020 was measured to be 1.542 at the wavelength of 1.3μm.

(2) Spin-coating the bottom dumping planer waveguide

We chose disperse red 1(DR1) side chained poly(methyl methacrylate) (PMMA/DR1, a polymer from IBM Almaden Research Center), as the NLO polymer. Because one end of the DR1 chromophore is covalently attached to the PMMA backbone, it has high nonlinearity. The maximum value of γ_{33} was reported to be ~22pm/v [33]. Under our poling conditions, it was ~12pm/v. Unlike the photo lime gel guest/host NLO polymer, PMMA/DR1 is not water-soluble. Thus creates an advantage in the device processing. The PMMA/DR1 solution was made by dissolving DR1 side-chained PMMA 0.2g into 1ml Cyclopentano solvent. The solution was then spin-coated on the substrate prepared in the previous step at the speed of 350rpm/sec. The film was then baked for 2 hours in 90°C oven. The film thickness was measured to be 5.1μm. The refractive indices of TE and TM mode of the film were measured to be 1.5762 and 1.5759 respectively at a wavelength of 1.3μm. We noticed that the refractive indices of TE and TM mode were almost the same before contact poling.

(3) Spin-coating buffer layer

In order for the light to be coupled from the guiding waveguide to the dumping planar waveguide, the separation between the guiding waveguide to the dumping planar waveguide should to be carefully controlled. As we have discussed in section 3.3.3, the dumping efficiency can be ~100% when the separation of the guiding waveguide from the dumping planar waveguide is 3μm. However, UV15

when the separation of the guiding waveguide from the dumping planar waveguide is 3μm. However, UV15 can no longer be used as the buffer layer because Cyclopentano,which is the solvent of PMMA/DR1, can penetrate through the UV15 buffer layer. We chose NOA61 as the buffer. It low loss at the wavelength of 1.3μm (~-1dB/cm) and is UV light curable. The refractive indices of TE and TM modes are 1.546 at the wavelength of 1.3μm, which is almost the same as the bottom cladding layer U9020. The spin-coating speed was 5000rpm. The thickness of the buffer layer was measured to be 2.7μm.

(4) Spin-coating the top core layer

In order to make the device as symmetrical as possible, the top core layer was made the same as the bottom dumping planar waveguide. The thickness of the top core layer was 5.1μm.

(5) Contact-poling of the film

In order to pole the top core layer efficiently, we deposited a thin Au layer (1100Å) directly on top of the top core layer. The Au layer worked as the top poling electrode, which made the poling voltage directly applied on the EO polymer film. The contact-poling voltage was 800V. The leakage current was measured to be 12μA. The poling temperature was 118°C, which is the Tg of PMMA/DR1. The detailed description of contact-poling of PMMA/DR1 film can be found in section 3.4. After contact-poling the poling electrode was removed using the Au etchant. Because the Au layer was very thin, the etching speed was very fast. Only several second was needed to remove the contact poling electrode.

(6) Defining of multi-mode waveguide channels

In order to form multi-mode waveguide channels, we defined channel patterns using the standard lithography technique. Positive photo resist AZ5209 was used to transfer the multi-mode waveguide patterns from the mask to the film. After lithography, the Reactive Ion Etching (RIE) technique was used to etch a rib structure as shown in Fig. 3.5.3. Photo resist AZ5209 was also used as the mask in RIE. The etching gas was O2 and the pressure was 20 mtorr. The etching time was 17 minutes. The height of the rib is measured to be 1.6μm. In this procedure, the photo resist AZ5209 was totally etched away. Therefore, it is not necessary to perform any additional steps to remove the photo resist.

(7) Forming of top cladding

Master Bond UV15® was used as the top cladding because it is UV curable. After poling, the sample was sensitive to temperature. When the temperature applied to the sample were near or above Tg of PMMA/DR1, the dipoles would relax to their random positions. Therefore no EO

coefficients would remain. The refractive indices of UV15® were 1.519 at 6328nm and 1.496 at 1.3μm.

(8) Patterning of top electrodes

The top heating electrodes were formed by a conventional wet etching method. A thin layer of Au (1100 Å) was first thermally deposited onto the surface of the sample. The sample was then spin-coated with a thin layer (1μm) of photo resist AZ5209. Next the photo resist was patterned using the lithography method. Finally, Au etchant was used to etch away un-wanted Au and thus form the electrodes. The length of the electrodes and that of the total device were 2.5 cm and 1.9 cm respectively.

3.5.3 Device testing

The device was then diced and edge-polished. In order to test the modulation properties of the device, the device was put onto the coupling-stage as shown on Fig. 3.3.11. A 1.3μm wavelength laser beam was TM polarized and then endfire coupled into the device through a 40X objective lens. The output light was focused through another 40X objective lens and then detected by a photo detector. The modulating voltage was generated by a function generator and then amplified by 40X through a voltage amplifier. The modulation curve (output power vs. modulation voltage) is shown in Fig. 3.5.4. The dot in this figure represents the experimental measurements and the solid line represents the fitting curve. The experimental measurements fits well with the cosine square modulation curve [22]. The dynamic range was measured to be 68V.

To measure the modulation depth, instead of using the photo detector, the output light was imaged onto a screen. An IR camera was used to obtain the near field real-time image, which was then collected by a computer and analyzed by a Spiricon™ beam analyzer. By comparing the output light power difference before and after applying modulation voltage of 50V, the modulation depth can be measured. Fig. 3.5.5 shows the output light images. When the modulation voltage was 0V, the output light power was 11.5e03mw. When the modulation voltage was 50V, the output light power was 9.75e02mw. Thus the modulation depth was be 31%. Fig. 3.5.6 shows the 3D view of the output light images. The peak in the central of the images was the output light from the guiding waveguide whereas the small peaks at the edge of the images represent the output light from the dumping planar waveguide.

Output
Power

Modulation voltage (V)
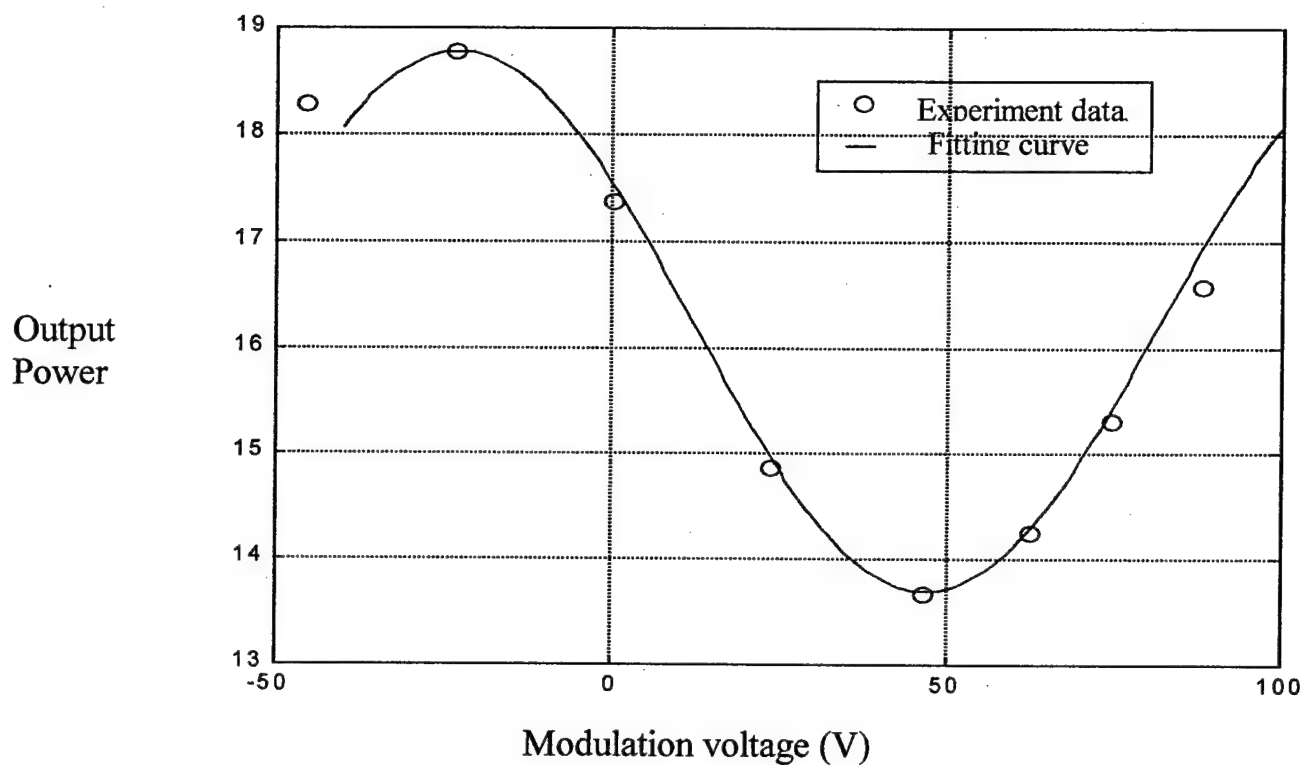
Fig. 3.5.4 Modulation curve of channel array EO modulator
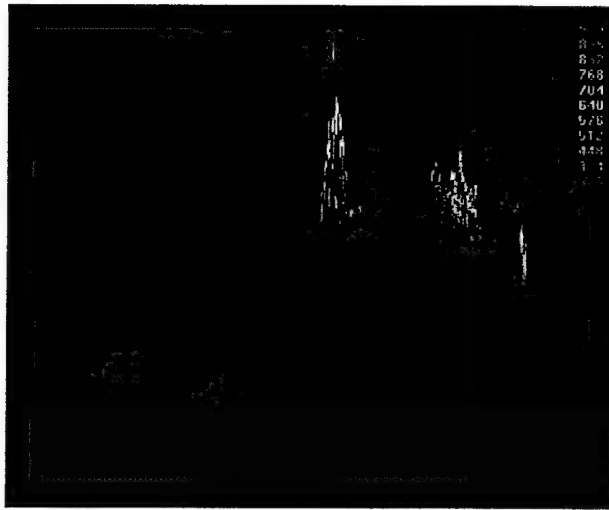

Fig. 3.5.5(a)
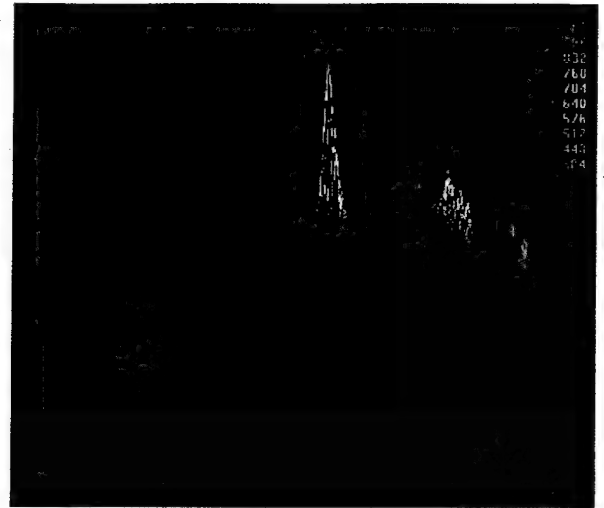

Fig. 3.5.5(b)

Fig. 3.5.5 2D view of modulation (a) V= 0V, (b) V = 50V

Fig. 3.5.6(a)   Fig. 3.5.6(b)

Fig. 3.5.6 3D view of modulation (a) V= 0V, (b) V = 50V

In order to measure the dynamic modulation of the device, an AC signal of peak-to-peak voltage of 40V was applied to the modulation electrodes of the device. The triangular form AC signal was chosen for the best display of the modulation curve. The frequency of the signal was 2KHz. A photo detector was used to measure the output light power of the guiding multi-mode waveguide. The output electric signal of the photo detector and the modulation AC signal were displayed on an simultaneously oscilloscope. Fig. 3.5.7, 3.5.8, and 3.5.9 show the dynamic modulation cure of the device. The upper trace was the tri-angular modulation signal and the lower trace was the response of the device.

Fig. 3.5.7 shows the modulation curve under the DC offset voltage of 10V. The output of the device increased as the modulation voltage decreased. When V_{AC} equaled $-36V$, the device reached its half wave voltage. A double frequency signal began to appear, which corresponds to the convex in the figure.
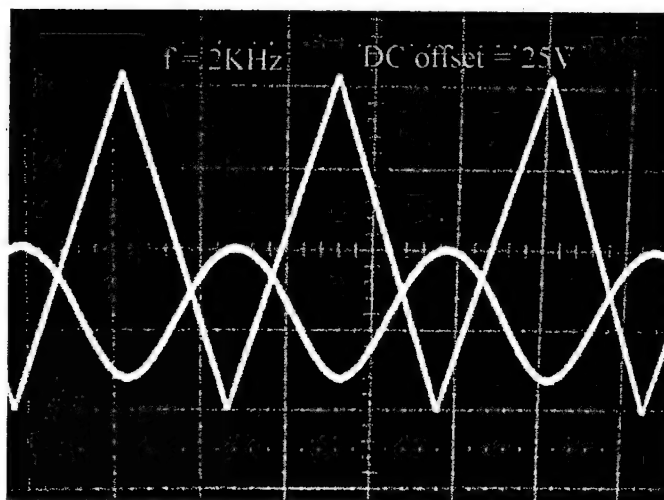
Fig. 3.5.8 shows the modulation curve under the DC offset voltage of 25 V. The output of the device increased as the modulation voltage decreased. Because the device is properly offset, the device performed cosine square modulation as described in other modulators [22].
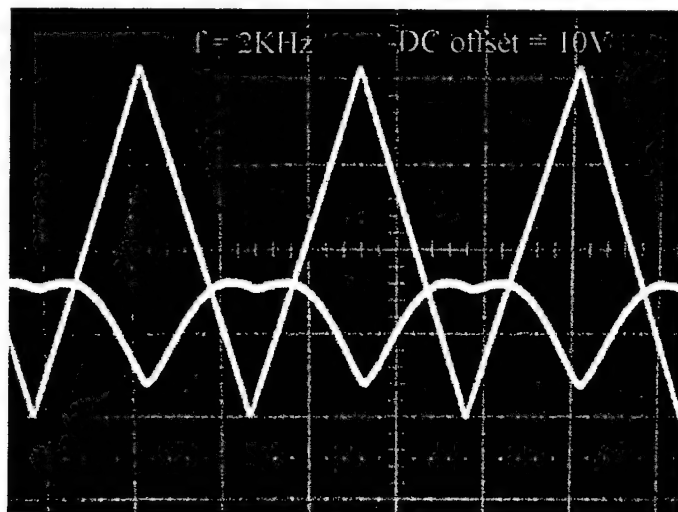
Fig. 3.5.7

Fig. 3.5.7 EO modulation Voff= 10V,Vpp = 40V

Fig. 3.5.8

Fig. 3.5.8 EO modulation Voff= 25V,Vpp = 40V

38

In order to examine how the response of the device under high modulation voltage, the peak-to-peak value of the tri-angular modulation signal was increased to 160V. The frequency of the modulation voltage was kept at 2Khz. Fig. 3.5.9 shows the device response of the modulation signal. Again, the upper trace was the tri-angular modulation signal and the lower trace was the response of the device. The figure clearly shows that when the modulation signal is high or low enough the device reaches half wave voltage. According to this figure, the modulation dynamic range was also measured to be ~70V.
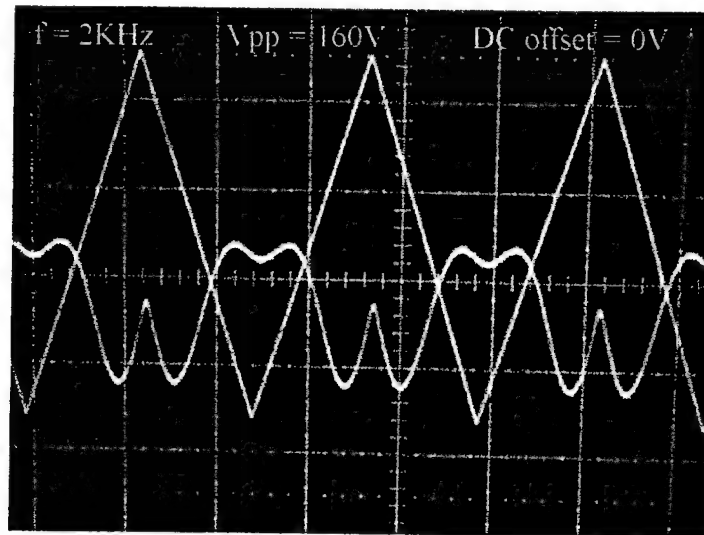
Fig. 3.5.9

Fig. 3.5.9 EO modulation Voff= 0V,Vpp = 160V
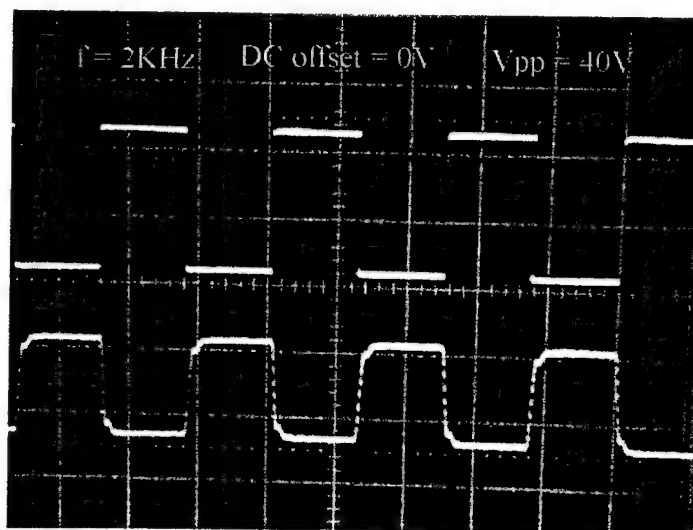
Fig. 3.5.10

Fig. 3.5.10 Step modulation Voff= 0V,Vpp = 40V

In order to examine the device's response to square wave modulation signal, a square wave modulation signal with a peak-to-peak value of 40V was applied to the modulation electrodes of the device. The frequency of the modulation voltage was kept at 2Khz. Fig. 3.5.10 shows the device's response to the modulation signal. Again, the upper trace was the square wave modulation signal and the lower trace was the response of the device. There were delays, estimated to be around 10μs, in both rising and falling edges. By improving the design of the modulation electrode structure, i.e. using traveling wave electrodes, the delay can be reduced to 1ns.
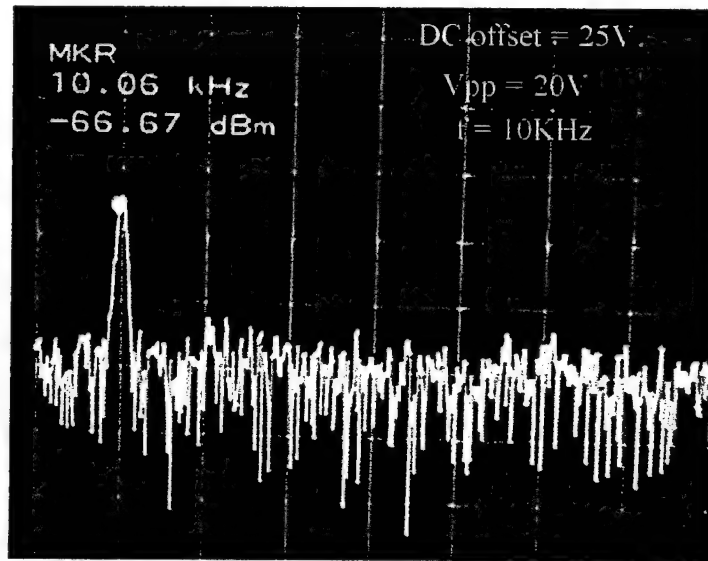

Fig. 3.5.11
Fig. 3.5.11 Spectrum of EO modulation Voff= 25V,Vpp = 20V

In order to examine the spectrum of the device's response to the tri-angular modulation signal, the tri-angular modulation signal with a peak-to-peak value of 20V was applied to the modulation electrodes of the device. The device was DC offset by 25V. The frequency of the modulation voltage was kept at 10Khz. The output of the photo detector was put through a spectrum analyzer. Fig. 3.5.11 shows the spectrum of the of the device's response to the tri-angular modulation signal. The detector's spectrum was only at 10KHz. No additional frequency was found, which shows good linearity when the peak-to-peak value of the modulation signal was 20V.

40

In order to measure the cross talk between adjacent channels on the Channel array Electro-optical modulator, the 1.3μm wavelength laser beam was TM polarized and then endfire coupled into one guide waveguide channel (channel 1)of the device through a 40X objective lens. The output light of an adjacent waveguide channel (channel 2) was focused through another 40X objective lens and then detected by a photo detector. By applying a modulating signal on the waveguide channel (channel 1), the output signal of channel was measured with regard to the modulating signal. The cross talk between the two channels was measured to be less than –22dB.

In summary, we designed, fabricated and tested a channel array multi-mode electro-optical modulator with vertically configured guiding channels and dumping layer. The device has a device packing density of 40 channels/cm. The modulation dynamic range was measured to be 68V. The modulation depth was 31%. The cross talk between adjacent channels was measured to be less than – 22dB.

4. SUMMARY OF THE RESEARCH

Through the course of the *high-performance unidirectional electro-optic modulator based on polymeric highly multi-mode waveguides* research, we have examined many issues that figure into determining the overall feasibility of the proposed research.

The most important concept in the research of modulators/switches based on multi-mode waveguide is the unidirectional coupling mechanism. In order to eliminate the degradation caused by the different coupling lengths of different modes in the multi-mode waveguide modulator, the coupling from the guiding waveguide to the dumpling waveguide has to be unidirectional. By exploring the unidirectional coupling mechanism, the switch extinction ratio of −21dB can be achieved as indicted by the thermal-optic switch experiment. The channel array multi-mode electro-optical modulator experiment also showed that the unidirectional coupling mechanism is feasible in building multi-mode waveguide modulators.

We have investigated two different device structures of the unidirectional multi-mode waveguides modulator. One is the coplanar multi-mode waveguides modulator, in which the multi-mode guiding waveguide and the multi-mode dumping waveguide were on the same layer. The coupling from the guiding waveguide to the multi-mode dumping waveguide is horizontal. The other is that the multi-mode guiding waveguide and the multi-mode dumping waveguide are vertically configured. Both of the structures can realize the unidirectional mechanism. The dumping efficiencies achieved were around 100%. The vertical configuration improves the device packing density by the factor of two. The EO modulator we made based on this vertically configuration has a device packing density of 40 channels/cm and the cross talk of less than −22dB. .

We have also investigated a novel polarization insensitive thermal optical switch based on the same multi-mode waveguide unidirectional coupling mechanism. The thermo-optic switch has an intrinsic wide optical bandwidth due to the large dynamic range of the phase-matching condition implied by the multi-mode waveguides. The thermo-optic switch is also polarization insensitive due to the direction independence of thermal effect ($\partial n/\partial T$).

We have explored different NLO polymers. The CR/photo lime gel guest/host polymer has extraordinary chemical and physical properties such as two-dimensional network and heat or UV curing The optical waveguides made of CR/photo lime gel guest/host polymer have low loss of less than 0.1dB/cm, as discussed in section 3.3.4. The refractive index of the polymer can be adjusted by changing the ratio of guest and host. The thermo-optic switch we made based on the CR/photo lime

gel guest/host polymer had an extinction ratio of −21dB. Disperse red 1(DR1) side chained poly(methyl methacrylate) (PMMA/DR1) is another polymer we examined in our research. This polymer was made by IBM Almaden Research Center. PMMA/DR1 is not water-soluble, which make it compatible with such VLSI processes as lithography, wet etch and edge polishing. This polymer has high nonlinearity due to the DR1 chromophore covalently attached to the PMMA backbone. The channel array multi-mode electro-optical modulator based on this polymer had a dynamic range of 68V.

We have developed a reliable contact poling method that can give sufficient EO coefficient for building EO devices. As discussed in section 3.4, compared with corona poling, the contact poling method has such advantages as precise poling voltage control, less surface damage and lower poling voltage. In order to improve the poling efficiency, the poling electrode was made directly on top of the NLO film. After contact poling, it was removed by Au etchant. During device fabrication, care must be taken to ensure that the defects due to material impurity be minimized. Otherwise, defects would cause short circuits during contact poling. The EO coefficient of 12pm/V was achieved using this contact poling method.

This research has proved by experiments and theoretical studies that the device *unidirectional electro-optic modulator based on polymeric highly multi-mode waveguides* presented in the proposal is feasible.

REFERENCES

1. P. G. Hunsperger, *Integrated Optics: Theory and Technology*, (Springer-Verlag, New York, 1984).

2. T. Tamir, *Guided-Wave Optoelectronics,* (Springer-Verleg, New York, 1988).

3. E. E. Bergmann, L. McCaughan, and J. E. Watson, Appl. Opt. **23**(17), 3000-3003 (1984).

4. W. K. Burns and A. F. Milton, IEEE J. of Quant. Electron. **QE-16**(4), 446-454 (1980).

5. J. C. Campbell, Appl. Opt. **18**(12), 2037-2040 (1979).

6. D. G. Sun and R. T. Chen, Appl. Phys. Lett., **72** (24), 3139 - 3141(1998).

7. Karl Joachim Ebeling, *Integrated Opto-electronics*, (Springer-Verlag, 1993)

8. Ray T. Chen, Optics & Laser Technology Vol. 25, No. 6, 347-365, 1993

9. Ray T. Chen, L. Sadovnik, T. Jannson, and J. Jannson, Appl. Phys. Lett. **58**, 1 (1991).

10. R. T. Chen, " Polymer based photonic integrated circuits," Optics & Laser Technology, Vol. **25**(6), 347-365 (1993).

11. B. L.Booth, "Low loss channel waveguides in polymer," IEEE J. Lightwave Technol. **7**, 1445 (1989).

12. R. T. Chen, M. R. Wang, C. Sonek, and T. Jannson, " Optical interconnection using polymer microstructure waveguides", Opt. Eng. **30**, 662 (1991).

13. C. T. Sulivan, A. Husain, "Guided-wave optical interconnections for VLSI systems," Proc. SPIE 881 (1988).

14. C. T. Sulivan, A. Husain, " Polymeric waveguide," IEEE Circuits and devices **27** (1992).

15. SPIE Vol. 1775 *Nonlinear Optical Properities of Organic Materials 369* (1992).

16. R.T. Chen, Proc. SPIE 1774, 20(1992).

17. Y.Shi, W. Wang, D. J. Olson, W. Lin, and J. H. Bechtel, Proc. SPIE 2852, 258(1996).

18. D. G. Girton, W. W. Anderson, J.A. Marley, T. E. Van Eck, and S. Ermer, OSA Tech. Dig. Ser. 21, 470 (1995).

19. Z. Z. Ho, Ray T. Chen, and Robert Shih, Applied Physics Letter, Vol. 61, No. 1, 4(1992).

20. Hyang-Mok Lee, Wol-yon Hwang, Min-cheol Oh, Heuk Park, and Taehyoung Zyung, Applied Physics Letters, Vol. 71, No. 26, 3779 (1997).

21. P. G. Hunsperger, *Integrated Optics: Theory and Technology*, (Springer-Verlag, New York, 1984).

22. T. Tamir, *Guided-Wave Optoelectronics,* (Springer-Verleg, New York, 1988).

23. E. E. Bergmann, L. McCaughan, and J. E. Watson, Appl. Opt. **23**(17), 3000-3003 (1984).

24. W. K. Burns and A. F. Milton, IEEE J. of Quant. Electron. **QE-16**(4), 446-454 (1980).

25. J. C. Campbell, Appl. Opt. **18**(12), 2037-2040 (1979).

26. D. G. Sun and R. T. Chen, Appl. Phys. Lett., **72** (24), 3139 - 3141(1998).

27. Karl Joachim Ebeling, *Integrated Opto-electronics*, (Springer-Verlag, 1993)

28. Ray T. Chen, Optics & Laser Technology Vol. 25, No. 6, 347-365, 1993

29. Ray T. Chen, L. Sadovnik, T. Jannson, and J. Jannson, Appl. Phys. Lett. **58**, 1 (1991).

30. Antao Chen, etc., Proc. SPIE 3281, 10 (1998).

31 Kenji Kitaoka, etc., Applied Physics Letters, Vol. 75, No. 2, 157(1999).

32. Huajun Tang and Ray T. Chen, Applied Physics Letters, Vol. 70, No. 5, 538(1997).

33. *"NLO Polymeric Waveguide Electro-Optic Phase Modulator,"* W.E.Moerner, D.Y. Morichere, A. Skumanich and B.A. Smith, SPIE Vol. 1775 Nolinear Optical Properities of Organic Materials V(1992), 369.